Title: Nav1.2 is a homeostatic sleep effector governing sleep quality

Authors: Yu Li[1*], Juhang Liu[1*], Kaiyue Yan[1*], Zhengbin Han[1], Chongchong Zhao[1], Laicai Zhang[1,2], Yanchen Liu[3], Mu Su[4], Bing Hu[1], Ying Li[1], Kaihang Ding[1], Tianmu Zhang[1], Hongyu Miao[1], Yikui Zhao[1], Huiwen Tian[1], Qiang Sun[1], Woo Jae Kim[1], Liang Li[2], Guangfu Wang[1†], Jing Ma[1†] and Zhiqiang Wang[1†]

Affiliations:

[1]The HIT Center for Life Sciences, School of Life Science and Technology, Harbin Institute of Technology, Harbin, Heilongjiang, China.

[2]State Key Laboratory of Space Environment Interation with Matters, Space Environment Simulation Research Infrastructure, Harbin Institute of Technology, 150080, Harbin, China.

[3]Beijing Institute of Genomics, Chinese Academy of Sciences, Beijing 100101, China.

[4]School of Life Science and Technology, Harbin Institute of Technology, Harbin, Heilongjiang, China.

[*]These authors contributed equally to this work.

[†]Correspondence:

Guangfu Wang: wangguangfu@hit.edu.cn

Jing Ma: jingmawzq@foxmail.com

Zhiqiang Wang: zhiqiang.wangmj@foxmail.com

Abstract:

Sleep is an evolutionarily conserved behavioral state critical for brain function and organismal health, with hundreds of genes linked to sleep regulation identified. However, the comprehensive molecular landscape of sleep, evolutionarily conserved functional processes, and therapeutically targetable signaling modules remain elusive. Here, we address these gaps *via* a multi-layered approach, constructing a quantitative sleep-regulatory network by integrating data from 217 mouse EEG/EMG-based studies, 156 *Drosophila* studies, and 25 phosphoproteomic datasets (10 sleep-related, 15 non-sleep). This analysis defines 115 sleep-regulatory genes (S-RGs), 293 sleep-associated phosphoproteins (S-PProts, including 16 S-RGs) and 479 well-annotated site-kinase pairs, while defining their hierarchical functional architecture and identifying neurotransmission, synaptic plasticity, and neuronal excitability as core processes governing sleep homeostasis. Notably, we reveal the unrecognized AKAP7α-RIIβ-PKA-Cα-Nav1.2 complex forms a compact homeostatic module: Nav1.2 undergoes time-dependent cumulative multisite phosphorylation that acts as a molecular timer encoding sleep pressure dynamics, whose slow inactivation gating kinetics directly fine-tuning neuronal excitability and thereby regulate NREMS slow-wave activity (SWA), the gold standard biomarker of sleep quality across multiple mouse models. We further establish direct translational potential: the FDA-approved drug gabapentin specifically enhances sleep quality by promoting Nav1.2 slow inactivation, validating this module as a highly specific, mechanism-based therapeutic target for sleep quality disorders.

MAIN TEXT

Sleep, a universally conserved behavioral state alternating with wakefulness, is essential for cognitive function, metabolic homeostasis, and survival[1-7]. Its complexity is reflected in measurable parameters: sleep-wake timing and architecture; durations of non-rapid eye movement sleep (NREMS), REMS, and wakefulness; signature brainwave patterns such as NREMS-SWA; and homeostatic rebound following sleep loss[8-10]. Optimal sleep requires balancing these interconnected parameters, yet our understanding of their molecular regulation remains incomplete, with profound clinical ramifications. Over 80 sleep disorders (e.g., insomnia, narcolepsy) affect hundreds of millions globally, but mechanism-based therapies are underdeveloped; most alleviate symptoms rather than targeting disease underpinnings[11,12].

Decades of research have identified two foundational pillars of sleep regulation: circadian clock molecules orchestrating sleep timing[11], and the orexin/hypocretin system governing arousal[12-14]. Technological breakthroughs (e.g., CRISPR/Cas9, AAV-mediated adult brain chimeric (ABC) analysis, high-throughput sleep phenotyping)[15-18] have accelerated the identification of hundreds of genes linked to sleep regulation[9,10,19-22]. Despite this progress, three key barriers hinder advancement beyond fragmented gene lists to a cohesive systems-level understanding:

First, no standardized quantitative framework exists to evaluate gene importance and functional specificity across distinct sleep parameters. Most studies focus on individual genes or phenotypes in isolation, precluding systematic comparison of their contributions to different traits, critical for distinguishing core regulators from peripheral modulators.

Second, the molecular and biochemical mechanisms linking genes to natural sleep physiology remain unknown. Most studies use genetic gain- or loss-of-function approaches, confirming a gene’s necessity or sufficiency but not how it is dynamically integrated into sleep-wake cycle fluctuations. This is critical because sleep is a whole-brain phenomenon: changes in cellular protein composition directly modulate neuronal excitability, a process unaddressed by static genetic manipulations.

Third, detailed analysis of sleep-wake cycle facets relies on quantitative electroencephalogram/electromyogram (EEG/EMG)-based sleep phenotyping. Unlike

automated noninvasive tools, mouse EEG recording requires invasive surgery and manual scoring, but it uniquely enables quantification of neurophysiological states, short EEG epoch power density, and specific brainwave patterns that are indispensable for dissecting sleep's molecular underpinnings. Notably, NREMS-SWA (EEG delta power, 1–4 Hz), the gold standard for assessing sleep need, depth, quality, and homeostasis, scales with prior wake duration and cognitive demand before decaying exponentially during sleep[23-25]. Genetic studies demonstrate substantial heritability of SWA dynamics[23], but the proteins and pathways orchestrating these temporal dynamics remain unresolved. This knowledge gap is clinically pivotal: sleep quality often matters more than duration for sustaining health and cognitive function.

Here, we address these three barriers through a multi-dimensional approach. We constructed a comprehensive quantitative atlas of sleep-regulatory molecular networks by integrating genetic perturbation data from mouse EEG/EMG datasets, and phosphoproteomic profiles. This work defines the hierarchical functional architecture of core sleep-regulatory components, filling the critical need for a standardized framework to evaluate the gene functions across distinct sleep phenotypes. Focusing on NREMS-SWA rebound after sleep loss, we identified the AKAP7α-RIIβ-PKA-Cα-Nav1.2 complex as a core sleep homeostasis module, which we have designated as the Hypnos Homeostatic Hub (HHH) complex. Cumulative phosphorylation of Nav1.2 dynamically modulates its slow inactivation kinetics, which in turn fine-tunes neuronal excitability to regulate sleep quality and thus establishes Nav1.2 as a pivotal molecular link between waking neuronal activity and homeostatic sleep responses. We further validate the translational potential of the HHH complex, as gabapentin enhances NREMS-SWA by directly targeting Nav1.2-dependent slow inactivation.

RESULTS

Constructing a quantitative sleep-regulatory gene atlas

Quantitative EEG/EMG-based sleep analysis enables detailed characterization of sleep-wake cycles **(Fig. 1a)**, which is critical for dissecting parameter-specific regulation. To date, hundreds of genes have been linked to distinct sleep traits, but no standardized framework evaluates their relative importance. We addressed this by collating 217 mouse EEG/EMG studies (1996–present) encompassing 355 genetic interventions across 196 unique genes. We further identified 139 genes from 245 interventions significantly associated with four key sleep parameters: NREMS duration, NREMS-SWA, sleep deprivation (SD)-induced NREMS time, and NREMS-SWA rebound **(Fig. 1b, Supplementary Table 1a and File 1)**. For cross-species validation, we analyzed 156 *Drosophila* studies (2000–present) involving 327 interventions, identifying 229 genes linked to basal sleep duration and SD-induced rebound. Of these, 206 *Drosophila* genes map to 303 mouse orthologs, providing initial evidence for evolutionary conservation of core-sleep regulatory components **(Fig. 1c, Supplementary Table 1b)**.

We next examined conservation at gene and functional levels **(Fig. 1d, e)**. Only 37 genes are shared between mouse and *Drosophila* orthologs **(Fig. 1d)**, but gene ontology (GO) analysis revealed ~50% of GO terms are conserved across three categories (cellular component, molecular function, biological process) with positive correlations (R^2>0.80) **(Fig. 1e, Extended Data Fig. 1a-c, Supplementary Table 2a)**. This resolves a longstanding paradox in sleep evolution: low conservation of individual sleep-regulatory genes but high functional similarity across species, confirming core sleep regulatory functions are evolutionarily retained despite divergent mediating genes.

Conserved genes fall into eight functional categories: (1) sleep regulatory substances (SRSs: TLR2/4, TNF-R1, 5-HT2A/2B/2C, etc.); (2) protein kinases (PKs: PKA-Cα/Cβ, LKB1, SIK3, ERK2), (3) protein phosphatases (PPPs: CnAβ/CnB, PTPRδ), (4) transcriptional regulators (TrRegs: CREB, TCF4/12, etc.), (5) ion channels (Cav2.1/2.3/3.3, Nav1.1, Kv1.2), (6) cell adhesion molecules (NLGN1/2/3), (7) circadian clock molecules (Clock, DEC2, REV-ERBα), and (8) miscellaneous regulators (FMR1, DISC1, NF-1, TAU) **(Fig. 1d)**. These genes are functionally enriched in signal transduction and neurotransmission **(Fig. 1d, e)**, supported by

97 cell-type-specific manipulations: pan-neurons (52 interventions) and excitatory neurons (32 interventions) drive most sleep modulations, with comparatively minor contributions from inhibitory neurons (4 interventions) and glial cells (astrocytes: 4, microglia: 2) **(Fig. 1f, Supplementary Table 1a)**. We further categorized 245 mouse interventions into 142 unique genetic manipulations (133 single-gene, 9 multiple-gene; total 139 genes) as loss-of-function (LOF, 123) or gain-of-function (GOF, 19). Notably, only 9 LOF interventions affect all four sleep parameters, while 14 LOF and 3 GOF impact three parameters **(Fig. 1g, Supplementary Table 1a)**. This uncovers two functional tiers: a core regulatory module coordinating global sleep homeostasis, and parameter-specific genes fine-tuning individual traits, revealing the modular organization balancing coordinated sleep-wake control with trait-specific regulation.

To prioritize relatively important genes, we collected raw data for all 245 interventions by directly quantifying published figures, standardizing to time difference (intervention minus control, minutes) and SWA fold change [(intervention minus control)/control, percentage] **(Fig. 1h, Extended Data Fig. 1d-g, Supplementary Table 1a)**. Using the 75th percentile as a predefined cutoff for impactful interventions (increased and reduced phenotypes), we identified 217 high-impact interventions critical for NREMS duration (137), SD-induced NREMS rebound (35), NREMS-SWA (91), and SD-induced NREMS-SWA rebound (45) **(Fig. 1i, Supplementary Table 1a)**. These map to 118 unique sleep-related interventions (S-Intervention, 111 single-gene, 7 multiple-gene) from 115 sleep-regulatory genes (S-RGs) **(Fig. 1j)**. We grouped these genes into 26 molecular subclasses **(Fig. 1i, Supplementary Table 1a)**, constructing the first quantitative sleep atlas that explicitly links molecular components to specific parameters, a resource guiding future mechanistic study.

Sleep quantity (duration) and quality (depth) are regulated by the balance between sleep homeostasis and circadian rhythmicity[3]. A homeostatic system comprises three core elements: a sensor monitoring the state variable, an integrator computing homeostatic drive, and an effector adjusting the variable[26]. Based on 115 S-RGs' molecular functions and top 10 S-Intervention, we proposed a phosphorylation-centered hierarchical model of sleep homeostatic signaling: (1) Sensors: SRSs (e.g. neuropeptides, neurotransmitters) and their receptors (e.g. NPSR1, 5-HT2C, mGluR5) detecting sleep need; (2) Integrators: PKs (e.g. PKA, CaMKII, SIK3) and PPPs (e.g. PP1, PP2A, calcineurin) processing sensory signals *via*

reversible phosphorylation; (3) Effectors: TrRegs (e.g. HDACs, CRTCs, FOS), ion channels (e.g. Kv3.1/3.3, Cav2.3, Nav1.2, Nav1.6), and synaptic regulators (SynRegs, e.g., SHANK3, SynGAP, VAMP2) modulating neuronal excitability and sleep phenotypes *via* transcriptional or electrophysiological mechanisms **(Fig. 1j, Extended Data Fig. 1h-l)**. This model positions reversible phosphorylation as a central integrative hub for sleep need signals, unifying diverse molecular observations into a coherent homeostatic framework.

Phosphoproteomic analysis defines the sleep-regulatory signaling network

The quantitative sleep-regulatory atlas identifies 17 kinases and 8 phosphatases as S-RGs **(Fig. 1i, Supplementary Table 1a)**, highlighting reversible phosphorylation as a central switch for sleep homeostasis. To delineate global kinase signaling dynamics, establish a phosphorylation-based regulatory network, and identify core hubs, we collated 25 published large-scale quantitative phosphoproteomic datasets (10 sleep-related, 15 non-sleep), enabling robust cross-paradigm validation **(Fig. 2a, Extended Data Fig. 2a, Supplementary Table 3)**. Sleep-related datasets include 7,343 unique phosphoproteins (PProts), 85,551 phosphopeptides (PPeps), and 55,182 phosphosites (PPsites)[25,27]. Non-sleep datasets (13,931 PProts, 81,119 PPeps, 70,088 PPsites) cover pharmacological models (bicuculline [BIC]-, tetrodotoxin [TTX]-, Ca^{2+}-, U50,488H [U50]-treated), stress models (chronic unpredictable mild stress [CUMS], forced swim stress [FSS]), mRNA splicing kinase SRPK2 manipulations (knockdown [KD] or overexpression [OE]), lipopolysaccharide (LPS)-treated bone marrow-derived dendritic cells (BMDCs), and ionizing radiation (IR)-treated A549 cells.

To evaluate global kinase signaling changes, we performed kinase motif-enrichment (KME) analysis covering 389 kinase motifs[28]. Pronounced kinase signaling perturbations were evident across most comparisons, which positively correlated with the number of significantly altered PPeps **(Fig. 2b, Extended Data Fig. 2b-f, Supplementary Table 4)**. Cross-correlation analyses revealed four key observations supporting kinase signaling's functional relevance in sleep regulation **(Fig. 2c, d, Extended Data Fig. 2g-j, Supplementary Table 5)**: (1) Eight increased sleep need comparisons showed concordant kinase signaling with positive pairwise correlations **(Fig. 2c, d)**; (2) Two decreased sleep need comparisons (pan-SIK inhibitor HG-9-91-0128 [HG]/vehicle [Veh] in WT and *Sleepy* mice) showed discordant signaling with negative correlations to increased sleep need **(Fig. 2d, Extended Data Fig. 2g)**; (3) Increased sleep need comparisons correlated positively with BIC-/Ca^{2+}-treated samples but negatively with TTX-treated samples, aligning with synaptic upscaling/downscaling **(Fig. 2d, Extended Data Fig. 2h-j)**; (4) No significant or negative correlations with other non-sleep datasets highlight a kinome-wide mechanism coupling calcium signaling, neuronal excitability, and synaptic plasticity to sleep homeostasis, which governs sleep-wake transitions.

To identify sleep-regulatory switch sites, we analyzed phosphopeptide change consistency across 10 sleep-related comparisons **(Fig. 2e, Extended Data Fig. 2k, Supplementary Table 6)**. We identified 462 high-impact sleep-associated phosphopeptides (S-PPeps) corresponding to 479 S-PPsites from 293 S-PProts (including 16 S-RGs) **(Fig. 2e, f and Extended Data Fig. 2k)**. These S-PPeps were significantly altered ($P<0.05$), exceeded the 75th percentile of log2(fold change) in 4 or more independent comparisons **(Fig. 2e)**, and their dynamics paralleled NREMS-SWA changes. Slimmed GO enrichment analyses showed 115 S-RGs and 293 S-PProts were significantly enriched in the functional categories of synapses, plasma membranes, cytoskeletons, and cytoplasmic vesicles, with the whole genome (16,190 genes) and all quantified PProts (8,068) serving as references **(Fig. 2g, Extended Data Fig. 2l, Supplementary Table 7)**. This supports the conclusion that synaptic strength remodeling is central to the core function and regulatory mechanisms of sleep. Phosphoproteomic analysis revealed more endosome-associated proteins but fewer mitochondrion- and extracellular region-related genes than S-RG enrichment **(Fig. 2g)**, highlighting inherent technical biases and complementary insights between genetic and phosphoproteomic approaches.

To characterize precise kinase-substrate site relationships, we adopted a hybrid prediction method combining KME and Group-based Prediction System (GPS)[28,29] to generate candidate kinase rankings for 479 S-PPsites **(Fig. 2h, Extended Data Fig. 2m, Supplementary Table 8)**. Manual annotation integrating prediction ranks and subcellular localization showed ~92% of annotated kinases were top 5 candidates **(Fig. 2h, Extended Data Fig. 2m)**. In total, 479 site-kinase pairs were mapped to 58 kinase families **(Fig. 2i)** and 128 individual kinases **(Extended Data Fig. 2n)**. These kinases, particularly top seven families (PKA, AMPKs, PKC, CaMKII, JNKs, ERKs, and AKTs) **(Fig. 2i)**, integrate brain state signals (cAMP, calcium, energy status, metabolism, stress) and transduce them *via* S-PProts phosphorylation to coordinate homeostatic sleep responses.

To uncover sleep regulation's hierarchical functional architecture, we integrated multiple functional datasets for representative S-RGs and S-PProts to construct a phosphorylation-based sleep regulatory signaling network **(Fig. 2j)**. This network reveals five key features: (1) Presynaptic synaptic vesicle exocytosis proteins are prominent S-PProts; active zone scaffolds (BSN, PCLO) emerge as key effectors encoding waking experience, linking kinase-induced phosphorylation to sleep need. VAMP2's robust sleep phenotype[30] confirms presynaptic protein importance and neurotransmitter release regulation as a core sleep control process. (2) CaMKIIα/β, mGluR5, SynGAP, and SHANK3 show cumulative phosphorylation and sleep phenotypes, alongside phosphorylation changes in synaptic cytoskeleton regulators (MAP2, SI1L1, BAIP2, MARK4), governing excitatory synaptic transmission and postsynaptic assembly, identifying them as core hubs mediating synaptic strength and sleep modulation. (3) Phosphorylation changes and sleep phenotypes were

detected for proteins involved in non-synaptic cytoskeleton organization, transcriptional/translational regulation, intracellular transport, proteostasis, mitochondrial function, and DNA damage responses, highlighting sleep's broad influence on cellular processes and the multifaceted nature of sleep regulation. (4) Plasma membrane proteins include many ion channel S-RGs, emphasizing neuronal excitability's importance for sleep modulation. Yet aside from Nav1.2, few ion channels exhibit strong sleep-dependent phosphorylation despite numerous phosphosites[31]. This striking selectivity strongly suggests that Nav1.2 serves a non-redundant, phosphorylation-gated role as a sleep homeostasis gatekeeper, distinct from other ion channels. (5) Broad kinase-substrate relationships and conserved sleep phenotypes associated with PKA, PKC, AMPKs (SIK1, SIK3, MARK4, BRSK1), AKTs, and CaMKII families highlight their roles as key signaling integrators; other kinases (PDHK1, CDK5, ATM/ATR) represent specialized regulatory modes, expanding sleep-regulatory complexity.

To date, only a handful of site-specific sleep regulatory functions have been characterized (e.g., PP2A-B56δ S565[6], CaMKIIβ T287) **(Fig. 2j)**. Each site-kinase pair's precise function requires further investigation using advanced biochemical and genetic approaches to decipher site-specific differentiation. Together, this comprehensive molecular landscape provides a novel conceptual framework and resource for decoding sleep regulatory and functional mechanisms at single PPsite resolution, bridging molecular phosphorylation events to systemic sleep homeostasis.

Sleep time-dependent cumulative phosphorylation of Nav1.2

Among sleep parameters, SD-induced NREMS-SWA rebound scales with the prior wake duration and decays exponentially during recovery sleep **(Fig. 3a)**. Genetic studies demonstrate considerable SWA dynamics heritability, and 39 S-RGs are linked to SD-induced NREMS-SWA rebound **(Fig. 1j)**; however, biochemical and electrophysiological mechanisms linking these S-RGs to physiological sleep homeostasis remain unresolved **(Fig. 3a)**. To identify proteins and pathways whose phosphorylation dynamics parallel NREMS-SWA rebound temporal changes, we analyzed 53,353 phosphopeptides from time-course SD (tc-SD; 0 h, 1 h, 3 h, 6 h), SD6/recovery sleep 3 h (RS3), and SD6/sleep 6 h (S6) phosphoproteomic datasets **(Fig. 3b, Extended Data Fig. 3a–d, Supplementary Table 9)**. This identified 310 sleep time-dependent phosphopeptides (STD-PPeps) from 215 unique STD-PProts **(Extended Data Fig. 3e, f),** exhibiting four distinct phosphorylation dynamic profiles **(Fig. 3c)**. Class A STD-PPeps (298) were dominant, paralleling NREMS-SWA: phosphorylation increased

during sleep loss ($P < 0.05$, slope > 0.2) and decreased during sleep **(Fig. 3b, c and Extended Data Fig. 3e)**.

Slimmed GO enrichment analyses showed 215 STD-PProts were significantly enriched in synapses, plasma membranes, cytoskeletons, and cytoplasmic vesicles relative to the entire quantified phosphoproteome **(Fig. 3d, Supplementary Table 7)**. Among 115 S-RGs, ten harbor STD-PPeps **(Fig. 3e)**, falling into two subgroups: mGluR5 (S901), CaMKIIα (T286), and CaMKIIβ (T287) harbor STD-PPeps and directly regulate SD-induced NREMS-SWA rebound; SynGAP (4 STD-PPeps), Nav1.2 (4), SHANK3 (3), CDKL5 (2), PP2A-B56δ (S81), δ-catenin (S200), and Cav2.1 (S2078) harbor STD-PPeps but have no reported role in this phenotype **(Fig. 2j)**. The sleep time-dependent phosphorylation of these proteins correlates closely with neurotransmission, synaptic plasticity, and neuronal excitability[2,25,30,31], highlighting these processes as central to sleep homeostatic control **(Fig. 3e)**.

Ion channels, as direct effectors, regulate neuronal firing, cortical network synchronization, global slow oscillations, and sleep homeostasis[31]. Among 80 sodium, potassium, and calcium ion channels, Kv3.1, Kv3.3, and Nav1.6 modulate SD-induced NREMS-SWA rebound **(Fig. 2j)** but lack sleep-dependent phosphorylation **(Fig. 3f)**; their mechanisms of sleep homeostatic regulation remain undefined. Nav1.1 (encoded by *Scn1a*) is another gene implicated in sleep regulation that promotes NREMS duration **(Supplementary Table 1a)** *via* inhibitory neurotransmission[32,33], and contains several sleep-related phosphopeptides **(Supplementary Table 3)**. However, both fell below our statistical cutoff and thus cannot be defined as S-RGs or S-PPeps **(Fig. 3f)**. Notably, Nav1.2 is the only ion channel in this cohort with four STD-PPeps, three clustering in its domain I–domain II (DI–DII) intracellular loop **(Fig. 3g)**. Consistent with this observation, numerous key phosphosites within the Nav1.2 DI–DII loop were upregulated in animal models of elevated sleep need and downregulated in those with reduced sleep need **(Extended Data Fig. 3g)**. Together, these observations reveal Nav1.2 is a unique, phospho-regulated electrophysiological effector that couples neuronal excitability to sleep homeostatic control *via* time-dependent phosphorylation[34,35].

Impaired Nav1.2 slow inactivation compromises sleep need

Heterologous expression studies establish that the Nav1.2 DI–DII intracellular loop is critical for slow inactivation: increased phosphorylation promotes slow inactivation, while mutation

of asparagine 1467 (N1467) in the domain III (DIII) S6 segment impairs this gating transition[36,37] **(Fig. 3h)**. To elucidate the roles of Nav1.2 cumulative phosphorylation and slow inactivation in sleep regulation, we generated *Scn2a*^{N1467D} mutant mice via CRISPR/Cas9 **(Extended Data Fig. 4a)**. However, homozygous *Scn2a*^{N1467D} mutants exhibited neonatal lethality within 48 hours **(Extended Data Fig. 4b)**, consistent with *Scn2a-null* mice[38]. In contrast, heterozygous *Scn2a*$^{N1467D/+}$ mice (*N1467D/+*) were healthy and fertile, with normal body weight and Nav1.2 protein levels **(Extended Data Fig. 4c, d)**. At baseline (BL), *N1467D/+* mice showed reduced NREMS-SWA despite normal total sleep duration **(Extended Data Fig. 4e-h)**; following SD, they showed a trend toward attenuated NREMS-SWA rebound and normal NREMS time rebound **(Extended Data Fig. 4i-k)**.

To establish a viable *Scn2a*^{N1467D} homozygous model, we generated an additional *Scn2a*$^{fl/fl}$ strain by inserting loxP sites downstream of exon 3 and upstream of exon 6 **(Extended Data Fig. 5a, b)**. We then crossed *Scn2a*$^{N1467D/+}$ and *Scn2a*$^{fl/fl}$ mice with CAGG$^{Cre-ERTM}$ transgenic mice, yielding two inducible strains: *Scn2a*$^{N1467D/fl}$*; CAGG*$^{Cre-ERTM/+}$ (*N1467D*) **(Fig. 3i)** and *Scn2a*$^{fl/+}$*; CAGG*$^{Cre-ERTM/+}$ strain (*KO/+*) **(Extended Data Fig. 5c)**. Two weeks after tamoxifen (TAM) induction (initiated at 6 weeks of age), Nav1.2 protein levels in both *TAM-N1467D* and *TAM-KO/+* mice were reduced to ~50% of those in WT and *N1467D/+* mice **(Fig. 3i, j; Extended Data Fig. 4c, 5d).** To confirm the Nav1.2 proteoform expressed in *TAM-N1467D* mice, we performed targeted sequencing of the Nav1.2 coding region (encompassing the N1467D mutation) using cDNA reverse-transcribed from cortical mRNA of WT, *N1467D/+*, and *TAM-N1467D* mice. Sequencing results confirmed that only the N1467D mutant mRNA was present in *TAM-N1467D* mice **(Extended Data Fig. 6a)**, verifying that *TAM-N1467D* mice exclusively express the Nav1.2 N1467D mutant proteoform.

NREMS-SWA is regulated in cerebral cortex layer 5 pyramidal neurons[9,10,24]. To assess how Nav1.2 N1467D mutation impacts channel slow inactivation *in vivo*, we performed whole-cell patch-clamp recordings on layer 5 pyramidal neurons from *ex vivo TAM-N1467D* and WT brain slices **(Extended Data Fig. 7c, d)**. Compared to WT, *TAM-N1467D* neurons exhibited significant slow inactivation impairments: sodium currents displayed impaired slow inactivation, delayed onset, and accelerated recovery across voltages **(Fig. 3k-n)**. *TAM-N1467D* mice exhibited normal EEG/EMG activity and body weight **(Extended Data Fig. 7a, b)**, as well as overall intact circadian wheel-running rhythms[35] **(Extended Data Fig. 6b-f).** This profile is distinct from that observed in *Scn2a*[35] or *Scn1a*[32,33] loss-of-function mouse models. These observations validate this strain as a reliable model for investigating the role of Nav1.2 slow inactivation in sleep regulation.

Detailed sleep-wake behavior analysis in *TAM-N1467D* mice revealed lower daily NREMS-SWA density **(Fig. 3o, p and Extended Data Fig. 7e)**, consistent with reduced baseline sleep need. Furthermore, SD6-induced NREMS-SWA elevation in WT mice was completely abolished in *TAM-N1467D* mice, whereas *TAM-KO/+* mice only exhibited a subtle reduction **(Fig. 3q, r and Extended Data Fig. 5i-k)**. Importantly, *TAM-N1467D* mice showed normal wake and NREMS durations **(Extended Data Fig. 7f-i)**, distinct from *Scn2a* homozygous knock out mice[35]. Together with observations from *N1467D/+* mice **(Fig. 3p, r)**, these results suggest Nav1.2 regulates sleep need in an allele-dose-dependent manner.

To confirm Nav1.2 functions in excitatory neurons to modulate NREMS-SWA, we performed ABC knockout *via* retro-orbital injection (ROI) of recombinant AAV-PHP.eB virus into adult *Scn2a*$^{N1467D/fl}$ mice **(Fig. 4a)**. This virus drives systemic CRE recombinase expression under either the *Camk2a* (excitatory neurons) or *mDlx* (inhibitory neurons) promoter. Consistent with *TAM-N1467D* mice, only *Camk2a-N1467D* mice exhibited reduced Nav1.2 protein levels **(Fig. 4b, Extended Data Fig. 8a)**, lower daily NREMS-SWA **(Fig. 4c, d and Extended Data Fig. 8b, g, h)**, and blunted SD-induced NREMS-SWA rebound **(Fig. 4e, f and Extended Data Fig. 8m)** with unaltered wake and NREMS durations **(Extended Data Fig. 8c-f, i-l)**.

To test whether Nav1.2 acts downstream of SLEEPY kinase, we expressed a constitutively active truncated SIK3 (sSLP), a well-established gain-of-function model of SIK3 *via* ROI of AAV virus carrying *Camk2a-HA-sSLP* **(Fig. 4g)**. Immunoblotting confirmed sSLP expression and elevated phosphorylation of the AMP-activated protein kinase (AMPK) substrate motif[6,25] **(Fig. 4h)**. Moreover, sSLP significantly enhanced Nav1.2 slow inactivation with voltage dependence, onset, and recovery changes opposite to *TAM-N1467D* mice **(Fig. 4i-l)**. As previously reported[6], forced sSLP expression in WT mice altered sleep-wake behaviors: shortened wake duration, increased NREMS duration, and elevated SWA during NREMS, REMS, and wakefulness **(Fig. 4g, m, o and Extended Data Fig. 9a-c)**. Notably, all sSLP-induced phenotypes were completely abrogated in *TAM-N1467D* mice **(Fig. 4n, o and Extended Data Fig. 9d-f)**, indicating that **the sleep-regulatory gain-of-function effects of SLEEPY are mediated through Nav1.2**.

Together, we show a single Nav1.2 amino acid mutation (N1467D) impairs slow inactivation, reducing baseline NREMS-SWA in WT mouse excitatory neurons, blunting SLEEPY-induced NREMS-SWA increases, and abolishing post-SD NREMS-SWA rebound. This phenotype is distinct from Nav1.2 knockout mice, which also affect NREMS duration **(Fig. 1i)**. Benchmarked against loss-of-function phenotypes of other S-RGs, Nav1.2 emerges as a pivotal effector of the sleep homeostatic system **(Fig. 4p, q)**.

Impaired Nav1.2 slow inactivation alters neuronal excitability

Given that impaired Nav1.2 slow inactivation compromises sleep need, we clarified its

electrophysiological mechanisms, specifically how this defect modulates neuronal excitability. We performed whole-cell patch-clamp recordings on layer 5 pyramidal neurons from *ex vivo* brain slices, applying 5-second prolonged current-step injections (20–240 pA) to monitor firing patterns **(Fig. 5a-g, Extended Data Fig. 10a-d)**. To establish a comparative framework, we included three control groups **(Extended Data Fig. 10e)**: (1) Nav1.2 homozygous knockout (KO) neurons, characterized by reduced baseline NREMS-SWA[35], increased action potential (AP) number, and decreased AP amplitude[39]; (2) sleep-deprived mouse neurons, which exhibit enhanced NREMS-SWA rebound, increased AP number, and unaltered AP amplitude[40]; and (3) WT and *TAM-KO/+* neurons as baseline controls **(Fig. 5a)**.

Relative to controls, *TAM-N1467D* neurons exhibited fewer AP spikes **(Fig. 5c)** and reduced AP amplitude **(Fig. 5f)** compared to WT and *TAM-KO/+* neurons during the initial 1-second epoch under weak depolarization (~120 pA). These differences gradually diminished with prolonged recording and increased current step **(Fig. 5d, g)**, disappearing at 200 pA depolarization **(Extended Data Fig. 10a-c)**. This unique phenomenon is largely attributable to time- and voltage-dependent slow inactivation of Nav1.2 in WT neurons or complete Nav1.2 protein loss in KO neurons[39], revealing a Nav1.2 slow inactivation-specific neuronal excitability regulatory mechanism **(Extended Data Fig. 10e)**. Together with NREMS-SWA findings and control group comparisons, these electrophysiological results suggest reduced AP amplitude and number induced by impaired Nav1.2 slow inactivation may contribute to decreased BL NREMS-SWA and attenuated SD-induced NREMS-SWA rebound, respectively **(Extended Data Fig. 10e)**.

To validate these observations transcriptionally, we performed bulk RNA sequencing (RNA-seq) on cortical *TAM-N1467D* neurons **(Fig. 5h, i and Extended Data Fig. 10f, Supplementary Table 10)**. This revealed modest transcriptional changes (0.35% of 15,104 genes), with downregulation of activity-dependent immediate early genes (IEGs; e.g., *Arc*, *Fos*, *Npas4*, *Nr4a1*, and *Egr2–Egr4*) **(Fig. 5i)**. This finding is consistent with reduced neuronal excitability, corroborating electrophysiological conclusions. Together, these electrophysiological and transcriptional findings demonstrate that Nav1.2 slow inactivation shapes cortical excitability in a time- and voltage-dependent manner, providing a cellular basis for its role in regulation of NREM-SWA and sleep homeostasis.

Nav1.2 functions as a homeostatic sleep effector

NREMS-SWA is regulated by intracellular kinase signaling in cerebral cortex excitatory

neurons[9,10,24]. Our prior quantitative phosphoproteomic analyses (sleep behavior-, sensor-, integrator-related datasets) revealed pronounced, correlated kinase signaling and phosphosite perturbations. Complementing these, quantitative EEG analyses identified Nav1.2 as a critical sleep homeostatic system effector downstream of behavioral and genetic manipulations **(Fig. 3 and 4)**. Together, these observations prompted us to delineate Nav1.2's molecular role in sleep homeostasis.

We performed quantitative proteomic and phosphoproteomic analyses on WT and *TAM-N1467D* mouse cerebral cortex samples under S6 and SD6 conditions **(Fig. 5h, Supplementary Tables 11 and 12)**. Relative to WT, *TAM-N1467D* samples showed specific ~30–50% reductions in Nav1.2 mRNA levels, protein abundance, and most Nav1.2-derived peptides **(Extended Data Fig. 10f-h)**, consistent with immunoblotting data **(Fig. 3j)**. We first compared the proteomes of *TAM-N1467D* and WT mice, quantifying 187,613 unique peptides from 12,341 proteins **(Extended Data Fig. 10g-h)**. Notably, very few proteins exhibited significant abundance changes, indicating the N1467D mutation minimally impacts global protein expression. Parallel phosphoproteomic analysis revealed that the mutation altered only a small fraction of the brain phosphoproteome: 5.3% of the total 35,246 phosphopeptides identified from 5,062 phosphoproteins **(**S6 condition; **Fig. 5j)**.

To clarify whether the N1467D mutation affects sleep-related signaling cascades and sleep need molecular substrates, we compared KME results and ΔPs values of sleep-need-index-phosphopeptides (SNIPPs)[25] between N1467D/WT and SD6/RS3 comparisons **(Fig. 5h)**. No parallel changes in altered kinase signaling or SNIPPs ΔPs values were observed in *TAM-N1467D* mice **(Fig. 5k–n, Supplementary Table 12)**, indicating attenuated Nav1.2 slow inactivation, rather than off-target effects on other sleep regulatory pathways, is the direct driver of decreased basal sleep need in *TAM-N1467D* mice.

We next evaluated whether the N1467D mutation impairs homeostatic responses to SD by analyzing SD6/S6 phosphoproteomic profiles between WT and *TAM-N1467D* mice **(Fig. 5o–s, Extended Data Fig. 10i–m)**. The phosphoproteome revealed striking genotype-specific plasticity in response to SD: WT mice exhibited significant SD-induced phosphoproteomic remodeling (9.5%), consistent with our prior findings[25] **(Fig. 5o)**, whereas this adaptive response was profoundly blunted in *TAM-N1467D* mice **(1.8%; Fig. 5p)**. Concordantly, SD-evoked kinase signaling alterations and SNIPPs cumulative phosphorylation, hallmark features in WT mice **(Extended Data Fig. 10i, k, m)**, were completely abrogated in *TAM-N1467D* mice **(Fig. 5q-s, Extended Data Fig. 10j, l)**. This stabilized phosphoproteomic state aligns with the widespread downregulation of IEGs, suppressed neuronal activity, and absent SD-induced NREMS-SWA rebound in *TAM-N1467D* mice, forming a coherent cellular and behavioral phenotype that specifically impacts SWA but not total sleep duration.

Collectively, these EEG, electrophysiological, and molecular findings converge across

multiple biological levels. Distinct, specific sleep quality alterations in *TAM-N1467D* mice—reduced basal NREMS-SWA and absent SD-induced NREMS-SWA rebound—demonstrate Nav1.2 functions as a downstream terminal effector in the sleep homeostatic system. Critically, Nav1.2 not only is regulated by sleep but also gates other sleep-associated signaling pathways, thereby governing sleep homeostasis and associated physiological processes.

AKAP7α-RIIβ-PKA-Cα-Nav1.2 forms a homeostatic sleep module

KME and GPS hybrid prediction identified seven PKA substrate sites within the Nav1.2 DI–DII loop **(Fig. 6a and Supplementary Table 13)**. This prediction was validated by immunoblot analysis using an antibody against the PKA-phosphorylated substrate motif (pPKAsub) following immunoprecipitation (IP) of endogenous Nav1.2 under S6 and SD6 conditions **(Extended Data Fig. 11a, b)**. Co-IP assays revealed that Nav1.2 interacts with the PKA catalytic subunit alpha (PKA-Cα), the PKA type II-beta regulatory subunit (RIIβ), and the membrane-anchored type II-specific A-kinase anchor protein 7 isoform alpha (AKAP7α) **(Extended Data Fig. 11c)**. We postulated that this AKAP7α-RIIβ-PKA-Cα-Nav1.2 complex mediates *in vivo* phosphorylation of Nav1.2 and the enhancement of slow inactivation **(Fig. 6b)**. To test this, we first administered Stapled AKAP Disruptor Peptide (STAD-2)[41] *via* intracerebroventricular injection (i.c.v.) at doses of 5 μg and 10 μg to disrupt AKAPs-RIIβ interactions **(Fig. 6b and Extended Data Fig. 12),** noting that STAD-2 is not Nav1.2-specific and can affect multiple AKAPs-RIIβ-associated substrates[41]. We found that 10 μg STAD-2 suppressed AKAP7α-RIIβ-Nav1.2 interaction, altered Nav1.2 phosphorylation **(Fig. 6c)**, and impaired Nav1.2 slow inactivation, recapitulating the key electrophysiological phenotypes observed in *TAM-N1467D* mice **(Fig. 6d-g)**.

Given the longitudinal design for sleep analysis, we quantified absolute EEG power within individual animals before and after drug treatment to avoid distortion by relative normalization, which can alter apparent band-specific effects *via* redistribution of total spectral power **(Extended Data Fig. 12a)**. We therefore compared NREM EEG power using absolute values. Consistent with molecular and electrophysiological changes, 10 μg STAD-2 significantly reduced baseline NREMS-SWA and the SD-induced NREMS-SWA rebound, without altering NREMS duration **(Fig. 6h–k; Extended Data Fig. 11d–h).** Notably, 10 μg STAD-2 altered absolute EEG power across all frequency bands (delta, theta, alpha, beta; **Extended Data Fig. 12b)**, whereas 5 μg STAD-2 had no significant changes **(Extended Data Fig. 12c–g).** These results suggest that additional downstream substrates contribute to the regulation of other frequency bands, since STAD-2 disrupts the association of RIIβ with multiple AKAPs.

To further validate the complex, we overexpressed Camk2a-driven RIIβ or AKAP7α in WT mice **(Extended Data Fig. 13a)** and found that only RIIβ overexpression significantly

increased NREMS-SWA without altering NREMS duration **(Fig. 6l–n; Extended Data Fig. 13b–g).** Finally, we generated Nav1.2 STD-PPsite triple mutant mice (*Scn2a*$^{S3A/+}$) harboring alanine substitutions at S573, S576, and S579 **(Extended Data Fig. 14a)**. These mice were crossed with *Scn2a*$^{fl/fl}$ mice to generate *Scn2a*$^{S3A/fl}$ progeny, then injected with *Camk2a-Cre* virus to yield the excitatory neuron-specific *Scn2a*$^{S3A/fl}$*; Camk2a-Cre (Camk2a-S3A)* line. **(Extended Data Fig. 14b)**. *Camk2a-S3A* mice exhibited reduced Nav1.2 protein levels **(Extended Data Fig. 14c)**, lower baseline NREMS-SWA, and a blunted SD-induced NREMS-SWA rebound, with normal wake and NREMS durations **(Fig. 6o-r and Extended Data Fig. 14d-h)**. These results establish that phosphorylation of the Nav1.2 DI–DII loop (at S573/S576/S579) provides a critical link between sleep-regulated kinases (including PKA and likely PKC family members) and Nav1.2 slow inactivation, directly mediating kinase-dependent control of homeostatic sleep need.

Collectively, these findings confirm that the AKAP7α–RIIβ–PKA-Cα holoenzyme complex acts as a sleep homeostatic integrator by promoting Nav1.2 phosphorylation in the DI–DII loop and enhancing its slow inactivation. We formally designate this AKAP7α–RIIβ–PKA-Cα–Nav1.2 assembly the Hypnos Homeostatic Hub (HHH) complex **(Fig. 6b)**, named for Hypnos (the Greek god of sleep) to reflect its role as a central homeostatic module that couples upstream signaling to the regulation of sleep quality.

Gabapentin improves sleep quality via Nav1.2 in mammals

Pioneering work on orexin/hypocretin, whose causal role in narcolepsy revolutionized understanding of arousal regulation, facilitated the development of orexin receptor antagonists, a new class of clinically approved sedative-hypnotics for insomnia[12-14]. Our results demonstrate that the HHH complex serves as a central regulator of sleep quality and identify Nav1.2 slow inactivation as a critical nodal point. This highlights Nav1.2 as a promising therapeutic target for mechanism-based treatments for sleep disorders.

Notably, Nav1.2 is a well-validated target for small-molecule modulators[42]. A prior study demonstrated that prolonged (3-day) administration of the clinical anticonvulsant gabapentin (GBP) induces a hyperpolarizing shift in the inactivation of rat Nav1.2 in heterologous cells[43]. Separately, a single intraperitoneal (i.p.) injection of GBP, administered before light onset, increased NREMS-SWA and prolonged NREMS duration in adult rats[44]. Clinically, GBP is also commonly used off-label to improve NREMS quantity in patients with primary insomnia[45], sensory nervous system disorders[46], and critical illness[47]. To validate the *in vivo* functional link between GBP, Nav1.2, and sleep homeostasis, we administered GBP *via* i.p. injection to WT and *Camk2a-N1467D* mice **(Fig. 7a)**. In WT mice, GBP significantly increased NREMS-SWA (first 3 hours) and NREMS duration (first 4 hours) in a dose-dependent manner **(Fig. 7b–e, Extended Data Fig. 15a–d)**. Notably, unlike the prolonged treatment required in heterologous systems, GBP rapidly enhanced Nav1.2 slow

inactivation in *ex vivo* cortical brain slices **(Fig. 7f–i)**, consistent with its acute sleep-modulating effects in animals. Critically, GBP-induced NREMS-SWA enhancement was completely abolished in *Camk2a-N1467D* mice, whereas GBP-mediated increases in NREMS duration were preserved **(Fig. 7j–m, Extended Data Fig. 15e–k)**. Collectively, these results indicate Nav1.2 is the key functional target for GBP-mediated regulation of sleep quality (NREMS-SWA), while an alternative target mediates its effects on sleep quantity (NREMS duration) in mammals. This provides the first direct *in vivo* evidence that Nav1.2 serves as a therapeutic target for improving sleep quality, thus validating the translational potential of our mechanistic findings.

Discussion

Sleep and wakefulness drive global phosphorylation changes in the brain proteome, with a subset tightly linked to sleep homeostasis regulation[7,25,27,48]. We previously hypothesized that molecular substrates of sleep need must meet the following criteria: accumulate during wakefulness, dissipate with sleep, track sleep pressure across contexts; be globally regulated in the brain; and their manipulation bidirectionally alters sleep need[25]. Nav1.2 fulfills all these criteria, revealing it as a unique, functionally specific molecular substrate that governs sleep quality in cortical excitatory neurons. This finding is consistent with recent cell-type-specific sleep studies[9,10,24] and supports its role as a critical terminal effector of the homeostatic sleep system (Fig. 7n).

Nav1.2 possesses three key molecular features that enable its function in sleep homeostasis regulation. First, multisite phosphorylation of Nav1.2 allows monitoring and integration of the quantity and complexity of prior wake experiences via activity- or use-dependent modifications, while mediating graded regulation of the channel's electrophysiological properties[36,37]. Second, as a voltage-gated sodium channel, Nav1.2 mediates action potential generation and backpropagation[34]. We propose that during sleep-wake cycles, dynamic phosphorylation fine-tunes its slow inactivation[36,37] to regulate neuronal firing dynamics, intrinsic and cortical network excitability. Sleep-dependent modulation of Nav1.2 slow inactivation stabilizes cortical slow oscillations and Up-Down states, thereby shaping NREMS-SWA. Nav1.2 thus acts as a cellular substrate linking sleep need to slow-wave homeostasis via dynamic gating, not overall excitability. Third, PKA is a key kinase in signal transduction pathways responsive to diverse SRSs that sense global neuronal activity. A similar scenario may apply to the PKC family, given our identification of Nav1.2 as a PKC substrate. Collectively, these three molecular features position Nav1.2 as a central signaling node that integrates kinase-dependent activity signaling with sleep homeostatic control.

It should be noted that both PKA and PKC are complex kinase families, whose activities are governed by distinct regulatory subunit compositions and subcellular localizations[49,50]. Thus, spatially restricted, compartmentalized kinase signaling modules that target specific

downstream effectors are required to delineate their authentic physiological functions. This targeted approach is far more informative than global kinase activity manipulation, which cannot resolve spatial or subunit-specific signaling differences.

Accordingly, the tightly membrane-anchored HHH complex likely forms a compact, cell-autonomous homeostatic module that serves as a paradigmatic example of the phosphorylation-based feedback regulatory system (PBFRs) logic governing sleep homeostasis. As a broadly conserved biological control principle, PBFRs are not unique to sleep; instead, they underpin diverse physiological and behavioral processes by enabling dynamic, activity-dependent adaptation[51-53]. In the context of sleep, the HHH complex represents a specialized molecular machine dedicated to the control of sleep quality, directly coupling activity-dependent kinase signaling to ion channel gating and neuronal excitability. Other PBFRs-based machineries—such as those involving Homer1a[7] or PERIOD proteins—likely contribute to distinct sleep-related processes, including synaptic plasticity and circadian timekeeping. Such PBFRs-based mechanisms control neuronal excitability, cortical network synchronization, and slow oscillations at both single-neuron and network levels[1,2] and operate *via* cell-autonomous feedback to maintain brain phosphoproteome balance, preserving optimal synaptic function, cognitive performance, and organismal survival[2,4,6,48].

From an evolutionary perspective, the core circadian mechanism, transcriptional-translational negative feedback loops (TTFLs), evolved to align with Earth's 24-hour rotation and regulate rest-activity cycles across most taxa[11]. A complementary, activity-dependent mechanism likely co-evolved to monitor cumulative neuronal activation, coordinate with TTFLs, and regulate vigilance states to maximize fitness. In animals, the nervous system consumes ~20% of total body ATP, primarily to sustain neuronal firing and synaptic transmission[54]. Meanwhile, phosphorylation dynamics of signaling transducers (e.g., S-PProts) fine-tune information processing in neural circuits, also at significant energetic cost. Viewed through the lens of both evolutionary necessity and first principles, phosphorylation emerges as particularly well-suited to serve as a core mechanism for sleep homeostasis. Beyond enabling rapid, reversible, and amplifiable signaling, multisite phosphorylation can accumulate and act as a graded regulator on specific proteins, extending the temporal range of functional changes beyond fast state transitions. This aligns with the need to encode both acute sleep-wake switches and the gradual build-up of sleep pressure over wakefulness. As fundamental units of cognition, neurons rely on both TTFLs and PBFRs to restore functional integrity for subsequent waking periods. Thus, the evolution of phosphorylation-based homeostatic mechanisms likely occurred in parallel with circadian TTFLs across animals to meet the demands of sleep-wake cycles.

Notably, PBFRs also operate within the circadian system: PERIOD proteins (PERs), core

circadian oscillator components, undergo robust circadian multisite phosphorylation modulated by CK1δ/ε-PP1 balance—a mechanism essential for TTFL progression[55]. Additionally, the KaiC phosphorylation cycle underpins the cyanobacterial circadian clock[56]. The discovery of RUVBL2[57], a eukaryotic KaiC analog with multiple phosphosites, suggests that phosphorylation-centered regulatory strategies are evolutionarily ancient and broadly conserved. While regulatory kinases, phosphatases, and effectors may differ—and act in distinct brain regions or cell types—the two-process model of sleep regulation[3] may converge upon PBFRs as a unifying core logic that integrates sleep homeostasis and circadian rhythms (Fig. 7n).

Intriguingly, several proteins function dually in both systems: for instance, SIK3 and HDAC4 modulate circadian arousal timing and period via the SIK3–HDAC4 axis in the suprachiasmatic nucleus (SCN)[58], and maintain sleep homeostasis while regulating NREMS amount and depth in the posterior hypothalamus or cortical neurons[9,10,19]. Nav1.2 was similarly reported to modulate circadian rhythms and SCN neuron spontaneous firing[35]. Our current data refine and extend this dual-function paradigm. We conclude that SCN-mediated circadian drive for wakefulness is functionally intact in our N1467D model, and the observed sleep homeostasis phenotypes are completely independent of SCN circadian function. These findings demonstrate that Nav1.2 slow inactivation is not required for circadian timekeeping, but instead serves as a specialized mechanism dedicated to sleep homeostasis control.

This distinction supports a unifying principle whereby core sleep–circadian regulatory proteins may control circadian timing and homeostatic drive through distinct molecular activities, in distinct brain regions, or in distinct cell types. Whereas Nav1.2 contributes to SCN pacemaking and circadian timing through other biophysical properties, its slow inactivation gating mechanism is uniquely specialized for sleep homeostasis—acting primarily in cortical or extra-SCN sleep-regulating networks. Thus, dissecting the PBFR regulators, effectors, and natural upstream sensors that interface with both sleep drive (homeostasis) and sleep–wake timing (circadian rhythms) will be critical to resolving how optimal sleep timing, duration, and depth are coordinated[3].

The discovery of the orexin/hypocretin system and subsequent development of its antagonists as sedative-hypnotics highlighted the transformative potential of mechanism-driven sleep research[12-14]. Similarly, our findings reveal the HHH complex as a potent, mechanism-specific regulator of sleep quality, acting through phosphorylation-dependent modulation of Nav1.2 biophysical properties. This pathway thus represents a promising, mechanism-based therapeutic target for next-generation sleep interventions to treat sleep disorders and their neuropsychiatric comorbidities. Our finding that gabapentin improves sleep quality by promoting Nav1.2 slow inactivation further validates this target. Next-generation derivatives with enhanced Nav1.2 specificity and optimized pharmacokinetics could therefore enable

619 precise, mechanism-based therapeutic modulation of sleep quality.

620

621

Acknowledgements

The authors thank Drs. Bing Fu and Shuhui Ji from the National Center for Protein Sciences (Beijing), the core facilities of the HIT Center for Life Science, and the Laboratory of Space Life Science under the Space Environment Simulation and Research Infrastructure for their kind technical assistance; Drs. Masashi Yanagisawa and Hiromasa Funato for providing the sleep analysis software.

This work was supported by grants from the National Major Project of China for Science and Technology Innovation 2030–Brain Science and Brain-Inspired Technology (2021ZD0203400 to Z.W.); the National Natural Science Foundation of China (32071011 to Z.W., 31970912 to G.W.); the National Key R&D Program of China (2022YFA1604502 to Z.W. and G.W.); the Lingang Laboratory & National Key Laboratory of Human Factors Engineering Joint Grant (LG-TKN-202203-01 to Z.W.); the Frontiers Science Center for Matter Behavior in Space Environment of China (to Z.W.); the Fundamental Research Funds for the Central Universities (HIT.DZJJ.2023132 to J.L.); and the startup funds from the HIT Center for Life Science.

Author Contributions

Z.W. conceived, designed, and supervised the project. Yu L., J.L., and J.M. performed the sleep experiments. Yu L., J.L., and C.Z. conducted the mass spectrometric experiments. K.Y., Yu L., and G.W. performed the electrophysiological experiments. Yu L., J.L., Z.H., L.Z., YC.L., M.S., B.H., Ying L., K.D., T.Z., H.M., Y.Z., H.T., Q.S., W.K. and L.L. completed all other experiments. Yu L., J.L., J.M., and Z.W. analyzed the data and prepared the figures. Z.W. wrote the manuscript with contributions from all other authors.

Materials and Methods

Quantitative analysis of sleep-regulatory genes

EEG/EMG-based sleep studies in mice were systematically curated from 1996 to the present. A total of 217 studies were included, encompassing 355 genetic interventions targeting four predefined key sleep parameters: NREMS duration, NREMS-SWA, SD-induced NREMS duration rebound, and SD-induced NREMS-SWA rebound. Interventions that significantly modified at least one of these parameters were retained, yielding 245 significant interventions corresponding to 139 genes (Supplementary Table 1a). For cross-species validation, 156 *Drosophila* sleep studies published since 2000 were compiled, identifying 327 interventions and 229 genes associated with baseline sleep duration or SD-induced rebound (Supplementary Table 1b).

To enable cross-study comparability, raw phenotypic values were extracted for all 245 mouse interventions. Values were recorded directly from text or tables, or digitized from graphical representations using WebPlotDigitizer v4.6 (https://plotdigitizer.com)[59] when presented only graphically. Time-related metrics were standardized as absolute differences between intervention and control groups (ΔTime = Time_intervention − Time_control; units: minutes). SWA-related metrics were standardized as relative percentage changes (ΔSWA = [(SWA_intervention − SWA_control)/SWA_control] × 100%). The 245 interventions were consolidated into 142 genetic manipulations (133 monogenic, 9 polygenic) and classified as loss-of-function (LOF) or gain-of-function (GOF). To address limitations of binary classifications, a standardized effect size distribution was employed to define “high-impact” interventions, with evaluations conducted separately for phenotypic increases and decreases. This identified 217 highly effective interventions corresponding to 115 sleep-regulating genes (S-RGs) and 118 sleep-related interventions (S-Interventions), which were functionally categorized into molecular subclasses to establish genotype-phenotype associations specific to sleep traits.

Cross-species GO enrichment correlation analysis

To assess functional conservation, we performed cross-species GO enrichment correlation analysis between mouse and *Drosophila* sleep-related datasets. The analysis was specifically conducted for mouse genes and mouse orthologs of *Drosophila* genes, using identical GO categories (Molecular Function, Cellular Component, Biological Process) and statistical parameters (Supplementary Table 2). GO terms significantly enriched (FDR < 0.05) in both analyses were retained for downstream comparison. For each shared term, enrichment scores from the mouse dataset were plotted against those from the *Drosophila*-ortholog dataset. Linear regression was used to quantify cross-species correlation, with the coefficient of determination (R^2) employed to assess the strength of functional concordance. The total number of enriched terms, overlapping terms, and regression statistics (slope, P value, R^2)

were reported for each GO category, enabling systematic evaluation of conserved biological functions underlying sleep regulation.

Kinase-motif enrichment analysis

To evaluate global kinase signaling changes across phosphoproteomic conditions, we performed paired kinase enrichment correlation analysis (Supplementary Tables 3–5). Details of the datasets used are listed in Supplementary Table 3. For each dataset, phosphopeptides were filtered by statistical significance ($P < 0.05$) and effect size based on $\log_2$(fold-change, FC). LFC cutoffs corresponding to the top 75% of $\log_2$FC values were determined independently to account for experimental variability. Significant phosphosites were extracted as 15-amino-acid sequence windows (7 residues upstream and downstream of the modified residue). Kinase-motif enrichment (KME) analysis[28] was then performed using the kinase-library Python package with the following parameters: kl_method = "percentile_rank", kl_thresh = 15, kin_type = "ser_thr", "tyrosine", enrichment_type = "enriched"[28]. Kinases with enrichment $P < 0.01$ were retained, ranked in ascending order of P value, and the top 75% were designated as significantly altered, accounting for variability in kinase detection and enrichment depth.

Pairwise comparisons of kinase enrichment profiles were conducted across all 25 phosphoproteomic datasets. For each pair, kinases significant in both datasets were identified, and their enrichment factors were subjected to linear regression-based correlation analysis. The regression slope, P value, and number of shared significant kinases were calculated for each comparison. Pairwise correlation results were visualized, with only correlations with $P < 0.05$ retained: positive correlations (slope > 0) were colored red, and negative correlations (slope < 0) were colored blue. Color intensity indicates the magnitude of the slope, and point size represents the number of shared significant kinases.

Identification of sleep-associated phosphopeptides

To identify phosphopeptides consistently associated with sleep-related conditions, we integrated ten independent sleep-related phosphoproteomic datasets. For each dataset, phosphopeptides were filtered by statistical significance ($P < 0.05$, retaining the top 75% most significant peptides by P value) and LFC magnitude (retaining the top 75% by $|\log_2$(fold-change, LFC)$|$), resulting in $\sim n \times 0.75 \times 0.75$ significant peptides per dataset. Phosphopeptides that were significant in ≥4 datasets and exhibited concordant directional changes were defined as sleep-associated phosphopeptides (S-PPeps). Concordance was defined as increased phosphopeptide abundance under high-SWA conditions (e.g., sleep deprivation, SD) and decreased abundance under low-SWA conditions (e.g., HG treatment), or vice versa (Supplementary Table 6).

A heatmap of all detected phosphopeptides was used to visualize the global significance of

each peptide across datasets, with columns representing the number of datasets in which each peptide was significant. Phosphopeptides significant in multiple datasets were thus positioned peripherally, while those with few or no significant hits were centralized **(Fig. 2e)**. For each S-PPep, the mean LFC across significant datasets was calculated separately for increasing and decreasing directions to characterize the magnitude and consistency of phosphorylation changes**.** A scatter plot was used to map the number of S-PPeps per protein-coding gene (x-axis) against the mean LFC of individual S-PPeps (y-axis) **(Extended Data Fig. 2k).**

GO slim enrichment analyses

To examine the subcellular localization patterns of S-RGs, S-PProts, and sSTD-PProts, we performed normalized distribution analysis based on GO Cellular Component (CC) slim terms (Supplementary Table 7). S-RGs, S-PProts, and STD-PProts were annotated to 12 predefined GO CC slim terms. For each GO CC term, the proportion of genes/proteins assigned to that term was calculated separately for each group (S-RGs, S-PProts, STD-PProts). To account for background detection biases, normalization was performed independently for each group using distinct reference sets: For S-RGs: Proportions in each GO CC term were normalized to the corresponding proportions in the full mouse genome (16,190 genes); For S-PProts and STD-PProts: Proportions were normalized to the corresponding proportions in the combined phosphoproteome derived from ten sleep-related phosphoproteomic datasets (8,068 genes).

Normalized values were further $\log_2$-transformed to facilitate quantitative comparison across different cellular compartments. This analytical approach enabled systematic quantitative assessment of the relative enrichment or depletion levels of sleep-related genes and phosphoproteins across major subcellular compartments.

Kinase prediction

Kinase predictions for each S-PPsite were obtained using two complementary methods: GPS[29] and KME[28]. Only kinases consistently identified by both methods for each S-PPsite were retained to improve prediction confidence. Candidate kinases were then ranked by relative KME scores in descending order. One kinase was manually assigned to each S-PPsite by integrating GO CC annotations of both the kinase and the corresponding S-PPsite (Supplementary Table 8).

Prediction performance was assessed based on the rank distribution of KME kinase scores:

91.65% of the predicted kinases were ranked ≤ 5, and 75% had KME kinase percentile scores > 92.16. For each S-PPsite, the mean LFC was derived from the maximum LFC values of the corresponding S-PPeps.

PKA substrate site prediction for Nav1.2 phosphosites was performed using two complementary methods: KME[28] and GPS[29]. For KME analysis, a percentile threshold of ≥ 95 was applied; for GPS, the high-confidence cutoff was used for both PKA subunits. GPS scores were subsequently normalized by subtracting their respective cutoffs (Fig. 6a). Predicted scores for all Nav1.2 phosphosites are provided in Supplementary Table 13.

Sleep time-dependent cumulative phosphorylation analysis.

Sleep time-dependent cumulative phosphorylation analysis was performed using two independent phosphoproteomic datasets: (i) time-course sleep deprivation (tc-SD: 0 h [baseline], 1 h, 3 h, 6 h SD) and (ii) acute SD (SD6, RS3, S6). Only phosphopeptides detected in both datasets were included for downstream analyses (n = 16,409).

STD-PPeps were defined as those exhibiting significant changes in either dataset, meeting two thresholds: (1) nominal $P < 0.05$ (retaining the top 75% of peptides with nominal $P < 0.05$) and (2) $|\log_2(\text{fold-change, LFC})|$ > 75th percentile of the LFC distribution. To characterize dynamic phosphorylation trends during tc-SD, linear regression was performed with SD duration treated as a continuous variable; peptides with $|\text{slope}| > 0.02$ and $P < 0.05$ were designated as exhibiting significant temporal trends.

Based on the regression slope direction (tc-SD) and phosphorylation changes (acute SD), STD-PPeps were classified into five groups (Extended Data Fig. 3e, Supplementary Table 9): slope^+ with decreased phosphorylation in RS3or S6 (A); slope^+ with increased phosphorylation in RS3 or S6 (B); slope^- with decreased phosphorylation in RS3 or S6 (C); slope^- with increased phosphorylation in RS3 or S6 (D); and peptides without consistent temporal trends (E).

Animals and genotyping

All animal experiments were conducted in accordance with protocols approved by the Harbin Institutional Animal Care and Use Committee of Harbin Institute of Technology (HIT/IACUC). Mice were of the C57BL/6J background, housed under controlled temperature and humidity with a 12-hour light–dark cycle, and given a*d libitum* access to food and water until 8-12 weeks of age for experiments. *Scn2a*^{N1467D}, *Scn2a*$^{fl/fl}$ and *CAGG*$^{Cre\text{-}ERTM/+}$ mice were purchased from Cyagen Bioscience (Guangzhou, China). *Scn2a*$^{S573A,S576A,S579A/+}$ *(Scn2a*$^{S3A/+}$*)* mice were generated in-house *via* CRISPR/Cas9-mediated genome editing[51].

CAGG$^{Cre\text{-}ERTM/+}$ were crossed with *Scn2a*$^{N1467D/+}$ to generate *Scn2a*$^{N1467D/+;\ Cre/+}$, which were then bred with *Scn2a*$^{fl/fl}$ to obtain *Scn2a*$^{N1467D/fl;\ Cre/+}$ mice. *Scn2a*$^{N1467D/+}$ were bred with *Scn2a*$^{fl/fl}$ to obtain *Scn2a*$^{N1467D/fl}$ mice. *Scn2a*$^{S3A/+}$ were crossed with *Scn2a*$^{fl/fl}$ to obtain *Scn2a*$^{S3A/fl}$ mice.

Genomic DNA was isolated from toe biopsies (postnatal day 8–12) using a commercial rapid genotyping kit (APE*BIO, K1025) containing lysis buffer, balance buffer, proteinase K, and 2× Taq PCR Master Mix. Tissue samples were incubated in 60 µL lysis buffer with 0.6 µL proteinase K (56 °C, 15 min), followed by inactivation (95 °C, 30 min), cooling to 4 °C, and neutralization with 60 µL balance buffer. PCR was performed with 0.5 µL lysate as template in 10 µL reactions. For *Scn2a*$^{N1467D/+}$ genotyping, PCR amplicons were digested with MboI (recognition site: GATC) in 20 µL reactions (10 µL PCR product, 3 µL buffer, 0.5 µL MboI, 6.5 µL ddH_2O) at 37 °C for 60 min. For *Scn2a*$^{S3A/+}$ genotyping, PCR products were digested with HaeII (recognition site: CGCG) under identical conditions. Digestion products were resolved by agarose gel electrophoresis, with genotypes assigned based on expected banding patterns.

EEG recording and sleep phenotype analysis

EEG recordings and sleep phenotype analysis were performed as previously described[6,8,19,25,60]. Custom-made electrodes consisted of an insulating base (7.62 × 6.08 × 8.26 mm) fitted with four gold-plated metal pins (0.50 × 0.40 × 2.6 mm) and two 15-mm Teflon-coated stainless-steel leads (Cooner Wire, #AS633). Two recording pins were positioned 5.08 mm anteroposteriorly and 2.54 mm mediolaterally. Gold plating was performed using Supermex #250 (Metalor Technologies).

Male mice (≥8 weeks old) were anesthetized with isoflurane, and their heads were secured in a stereotaxic frame. The scalp was shaved and disinfected with 3% hydrogen peroxide. Using bregma as the origin (0, 0, 0), four skull holes were drilled at the following coordinates: (−1.27, 0), (−1.27, 5.03), (1.27, 5.03), and (1.27, 0) mm. Stainless steel screw electrodes were implanted and affixed to the skull with dental cement (3M), followed by scalp suturing. Mice were individually housed for a 7-day recovery period, followed by an additional 7 days of habituation to the recording cables and setup. Sleep deprivation (SD) was conducted from Zeitgeber Time 0 (ZT0) to ZT6 using an automated orbital shaker, with *ad libitum* access to food and water provided throughout.

EEG and EMG signals were acquired using a multichannel amplifier (NIHON KODEN, AB-611J), band-pass filtered (EEG: 0.5–100 Hz; EMG: 0.5–300 Hz), and digitized at 250 Hz using a National Instruments PCI-6220 analog-to-digital converter controlled by LabVIEW software. Data were scored semi-automatically in 20-second epochs, followed by rigorous manual correction to ensure accuracy. Wakefulness was defined by low-amplitude fast EEG and high-amplitude EMG activity; NREMS by high-amplitude delta (1–4 Hz) oscillations and low muscle tone; and REMS by dominant theta (5–8 Hz) activity and muscle atonia. Fast Fourier transform was applied to EEG data (1–30 Hz).

For longitudinal analyses (e.g., SD-induced NREMS-SWA rebound, drug treatment responses), absolute EEG power was used to avoid normalization-induced distortions and to

detect within-subject changes. For cross-sectional comparisons between genotypes, relative power (%) (power in each frequency band divided by total power) was used to minimize variability arising from skull thickness, bone impedance, and electrode placement[8,25,61]. Hourly averages (ZT0–ZT23) of sleep stage durations and power density were calculated. All analyses were performed by experimenters blinded to mouse genotype. Mice with unreadable EEG signals were excluded post-hoc to ensure data quality.

Cannula implantation and drug administration

Male mice (≥8 weeks old) underwent intracerebroventricular cannula implantation under isoflurane anesthesia, with heads secured in a stereotaxic frame. Bregma (0, 0, 0) was used as the origin. Burr holes were drilled, and a cranial cannula implanted at (2, –0.5, –1.45) with a 30° insertion angle. Electrodes were implanted at (−1.77, 0, 0), (−1.77, 5.03, 0), (1.77, 5.03, 0), (1.77, 0, 0). STAD-2[41] (HY-P2261, MCE) was dissolved in DMSO to prepare a 200 μg/μL stock solution, diluted with sterile physiological saline (0.9% saline), and administered *via* intracerebroventricular injection at ZT23 (5 μg and 10 μg). Tamoxifen (S1238, Selleck) was dissolved in corn oil (20 mg/mL). At 6 weeks of age, $Scn2a^{N1467D/+;\ Cre/+}$ mice and littermate $Scn2a^{fl/+}$ mice received intraperitoneal tamoxifen (75 mg/kg) for 5 consecutive days. Tamoxifen treatment did not affect body weight in either genotype. Gabapentin (PHR1049, Sigma) was dissolved in 0.9% saline (3 mg/mL, 12 mg/mL) and administered intraperitoneally at ZT23.5 (30 mg/kg, 120 mg/kg).

cDNA amplification and Sanger sequencing

Adult mouse brains were rapidly dissected, immediately transferred into RNAiso Easy reagent (TAKARA, RNAiso Easy kit, TCH020) and homogenized. All procedures were performed in accordance with the manufacturer's instructions. First-strand cDNA was synthesized from purified mRNA using a reverse transcription kit (TAKARA, PrimeScript™ RT Reagent Kit with gDNA Eraser, RR047A). A primer pair spanning the exon 21–22 junction was designed to specifically amplify the spliced transcript. PCR amplification was carried out using cDNA as the template, with the forward primer (5′-CTCTGCTTCAAGTAGCCACATTTAAAGG-3′) and a custom reverse primer (5′-CATCCCTTGAAACTTGTTAGCAGGGC-3′). Amplified products were gel-purified and subsequently subjected to Sanger sequencing.

Circadian locomotor activity analysis

Wheel-running activity was recorded in cages equipped with low-resistance running wheels, binned at 5-min intervals, and analyzed using ClockLab software (Actimetrics). Mice were singly housed and maintained under a stable 12 h light : 12 h dark (LD) cycle for at least 7 days to achieve circadian entrainment. Animals were then transferred to constant darkness (DD) and kept in DD for at least 10 days before being returned to a 12 h : 12 h LD cycle. Circadian period was determined using χ^2 periodogram analysis in ClockLab. Rhythm

amplitude was estimated from the strength of the dominant circadian component. All analyses were performed using activity data collected exclusively during the DD phase to minimize masking effects of external light cues.

Brain slice preparation and electrophysiology

Motor cortical slices for electrophysiological recordings were prepared per established protocols[62,63]. Whole-cell patch-clamp recordings were conducted at 32–34 °C using Model 2400 amplifiers (A-M Systems) and MultiClamp 700B Microelectrode Amplifier (Molecular Devices), with data analyzed by Igor Pro 6 (WaveMetrics). Brain slices from 8-week-old mice were prepared by decapitation, rapid brain extraction, and immersion in ice-cold artificial cerebrospinal fluid (ACSF: 119 mM NaCl, 2.5 mM KCl, 1 mM NaH_2PO_4, 26 mM $NaHCO_3$, 1 mM $MgCl_2$, 25 mM glucose, 2 mM $CaCl_2$; pH 7.4, 300–305 mOsm, saturated with 95% O_2/5% CO_2). For recordings from gabapentin-injected WT mice (120 mg/kg), 300 μM gabapentin was added to ACSF. Brain tissue was mounted on a 10° bevel slicing platform and cut into 400 μM coronal sections using a VT1200S vibratome (Leica Biosystems). Slices were incubated in oxygenated ACSF (37.0 °C ± 0.5 °C, 20 min), then at room temperature until transfer to the recording chamber.

Recordings were obtained from layer 5 pyramidal neurons in the motor cortex. Electrodes (4–7 MΩ) were pulled from borosilicate glass using a P-97 puller (Sutter Instruments). Intracellular solution for slow inactivation recordings contained 10 mM HEPES, 2.5 mM $MgCl_2$, 20 mM CsCl, 115 mM $CsMeSO_3$, 4 mM Na_2-ATP, 0.4 mM Na-GTP, 10 mM Na-phosphocreatine, 0.6 mM EGTA, 0.1 mM spermine (pH 7.25, 300 mOsm/kg). Intracellular solution for neuronal excitability recordings contained 120 mM potassium gluconate, 10 mM HEPES, 4 mM KCl, 4 mM MgATP, 0.3 mM Na_3GTP, 10 mM sodium phosphocreatine (pH 7.25, 300 mOsm/kg). A motorized micromanipulator (Junior Multpatch, Lugis & Neumann) guided electrodes to target cells. Data acquisition and stimulation were controlled by Igor Pro 6 via synchronized LIH 8+8 interface boards (HEKA Instruments).

For voltage dependence of slow inactivation: a 5-s prepulse from −100 mV to between −120 mV and −20 mV, repolarization to −100 mV (20 ms), and a 10-ms test pulse to 10 mV. For onset kinetics: a fixed 10 mV prepulse with exponential durations (10 ms–$10^{3.8}$ ms). For recovery kinetics: a fixed 10 mV/5 s prepulse with variable interpulse intervals. Neuronal excitability was assessed by depolarizing step currents (25 steps, 0.02–0.24 nA, 5 s). AP waveforms and amplitude (first/last epoch) were recorded at 120 pA and 200 pA.

Immunoprecipitation and immunoblotting.

Brain tissue was rapidly excised, snap-frozen in liquid nitrogen, and stored at −80 °C. Glass homogenizers and lysis buffer were pre-cooled. Lysis buffer contained 1% Triton X-100, 150 mM NaCl, 20 mM HEPES (pH 7.4), 2 mM $MgCl_2$, 1 mM EDTA, 15 mM NaF, 20 μM leupeptin hemisulfate, 10 μM pepstatin A, 1 mM PMSF, 100 mM sodium orthovanadate, 4

mM sodium tartrate dibasic dihydrate, and a protease-phosphatase inhibitor cocktail. Brain tissue was homogenized in 4 mL lysis buffer with nuclease (#88702, Thermo) at 4 °C, incubated on ice for 30 min, and centrifuged (13,000 g, 20 min, 4 °C) to collect supernatant. Protein concentration was determined by BCA assay. For immunoprecipitation, 35 mg protein was pre-incubated with 30 µL Protein A/G PLUS-Agarose (sc-2003, Santa Cruz) (4 °C, 30 min), centrifuged (2,500 rpm, 5 min, 4 °C), and supernatant collected. Anti-SCN2A (Nav1.2) (#ASC-002, Alomone Labs; 5 µL) was added to supernatant (4 °C, 1 h), followed by 30 µL Protein A/G PLUS-Agarose (4 °C, overnight) to isolate immune complexes. Protein samples were separated by SDS-PAGE and analyzed by Western blotting.

Immunoblotting used the following primary antibodies: anti-SCN2A(Nav1.2) (1:1000, #ASC-002, Alomone Labs), anti-β-Tubulin (9F3) (1:1000, #2128, Cell Signaling), anti-GAPDH (14C10) (1:1000, #2118, Cell Signaling), guinea pig anti-SCN2A(Nav1.2) (1:1000, ASC-002-GP, Alomone Labs), anti-phospho-AMPK Substrate Motif (LXRXX(S*/T*)) (1:1000, #5759, Cell Signaling), anti-phospho-PKA Substrate (RRXS*/T*) (1:1000, #9624, Cell Signaling), PRKAR2B polyclonal antibody (1:1000, 28351-1-AP, Proteintech), DYKDDDDK Tag (D6W5B) Rabbit mAb (1:1000, #14793, Cell Signaling), anti-Cre Recombinase (D7L7L) (1:1000, #15036, Cell Signaling), PKA C-α antibody (1:1000, #4782, Cell Signaling), anti-HA (C29F4) (1:1000, #3724, Cell Signaling), and anti-AKAP7 (1:1000, 12591-1-AP, Proteintech).

Plasmids construction and AAV packaging.

Mouse sSLP ORF (Sik3, A260–K527, NM_027498) was obtained from Comate Bioscience. Human AKAP7α and pAAV-Camk2a-PRKAR2B-3×FLAG were purchased from Miaoling Biology (P4655, P80292). pAAV-Camk2a-AKAP7α-3×FLAG was generated by replacing PRKAR2B in pAAV-Camk2a-PRKAR2B-3×FLAG with AKAP7α. Cre recombinase and mDlx promoter were from pAAV-U6-sgRNA-pCBh-Cre-WPRE-hGHpA (60229, Addgene) and pAAV-mDlx-GFP-Fishell-1 (83900, Addgene). pAAV-Camk2a-Cre and pAAV-mDlx-Cre were constructed by restriction enzyme digestion and ligation.

AAV packaging and purification were performed as previously described with modifications[6]. pAAV-PHP.eB[64], pAAV-helper, and target gene-containing pAAV vector were co-transfected into AAVpro 293T cells using PEI MAX. Twelve hours post-transfection, medium was replaced with serum-free DMEM. After 5 days, supernatant was collected and cells harvested. The mixture was centrifuged (13,000 rpm, 10 min, RT), and supernatant transferred to a new tube. Cell pellets were resuspended in 1 mL PBS, subjected to 5 freeze-thaw cycles, and centrifuged (13,000 rpm, 20 min) to collect supernatant. Combined supernatants were filtered (0.45 µm) and mixed with 6 mL 14% BSA (3% final concentration) and 7 mL pre-chilled 4× PEG8000, then incubated at 4 °C overnight. Samples were centrifuged (3,500 g, 1 h, 4 °C), supernatant discarded, and pellets resuspended in 1.5 mL PBS. Concentrated virus was stored

at −80 °C. Titers were determined using linearized genomic plasmids as standards. Mice were anesthetized with isoflurane and injected with 100 µL AAV (1.0×10^{12} vg/ml) via retro-orbital sinus.

Transcriptomic analysis.

Cerebral cortex and hippocampus from tamoxifen-induced mice (10 days post-induction) were rapidly dissected, snap-frozen in liquid nitrogen, and sent to Novogene for sequencing. Total RNA was extracted using TRIpure Isolation Reagent (94015120, Roche). For each sample, 1 µg RNA was used for library preparation with the NEBNext® Ultra™ RNA Library Prep Kit for Illumina® (NEB), and index codes added. Libraries were clustered on a cBot Cluster Generation System (TruSeq PE Cluster Kit v3-cBot-HS, Illumina) and sequenced on an Illumina HiSeq X Ten platform (150 bp paired-end reads). High-quality reads were aligned to the mouse reference genome (GRCm38, Ensembl release 90) using Hisat2 (v2.0.4), with gene expression quantified by HTSeq (v0.9.1).

Raw sequencing data were quality-checked by FastQC. Gene expression analysis was performed with edgeR. Lowly expressed genes (≥20 counts in ≤40% samples) were filtered. Normalization was done using the trimmed mean of M-values (TMM) method. Dispersion estimates were obtained, and gene expression modeled by generalized linear models. Differential expression was assessed by likelihood ratio tests. Differentially expressed genes (DEGs) were defined as FDR < 0.05 and $|\log_2$ fold-change$| > 1$ (Supplementary Table 10).

Tissue collection and sample preparation for mass spectrometry.

WT and *Scn2a*^{N1467D} mice were subjected to 6 h normal sleep (S6) or 6 h SD (SD6). Brains were rapidly excised, snap-frozen in liquid nitrogen, and stored at −80 °C[25]. Brain tissue was lysed in buffer containing 50 mM HEPES (pH 8.5), 150 mM NaCl, 2 mM $MgCl_2$, 1% SDS. Tissue was homogenized in 5 mL lysis buffer with nuclease (Thermo) and 2 mL 10% SDS, incubated for 30 min, and centrifuged (13,000 g, 20 min, RT) to collect supernatant. Protein concentration was determined by BCA assay. Lysates were reduced with dithiothreitol, alkylated with iodoacetamide, precipitated with chloroform-methanol, and resuspended in 8 M urea. Samples were digested with recombinant Lys-C (2 h), diluted to 2 M urea with 100 mM NH_4HCO_3 (pH 7.8), and digested with trypsin (Promega, RT, 12 h). Digestion was terminated with 1% trifluoroacetic acid (TFA). Peptides were desalted by C18 solid-phase extraction and concentrated by vacuum centrifugation.

Desalted peptides were resuspended in 1.2 mL phosphopeptide binding buffer (2 M lactic acid/50% ACN), centrifuged (13,000 g, 20 min), and supernatant collected. TiO_2 beads were washed three times with binding buffer, added to supernatant (RT, 1 h), and washed twice with 2 M lactic acid/50% ACN and twice with 50% ACN/0.1% TFA. Phosphopeptides were eluted twice with 500 µL 50 mM K_2HPO_4 (pH 10), acidified with 20% TFA, desalted, and concentrated.

Enriched phosphopeptides were resuspended in 200 mM HEPES (pH 8.5), with concentration determined by BCA assay. ~50 µg of each sample was labeled with Tandem Mass Tags (TMT) (RT, 1 h), quenched with 5% hydroxylamine, pooled, acidified with 20% TFA, desalted, and concentrated. Samples were fractionated by HPLC (Agilent 300 Extend C18 column) with buffer A (1% ACN, 10 mM ammonium formate, pH 9.5), acidified with 20% TFA, concentrated, desalted by Stage Tips, and resuspended for LC/MS analysis.

Mass spectrometry data acquisition and processing.

TMT-labeled peptides were separated by 120-minute gradient elution (0.300 mL/min) via an Ultimate 3000 system connected to a Thermo Orbitrap Exploris 480 mass spectrometer. The analytical column was a fused silica capillary (75 µm ID, 150 mm) packed with C-18 resin (300 Å, 5 µm; Varian). Mobile phase A: 0.1% formic acid; mobile phase B: 100% ACN/0.1% formic acid. The spectrometer was operated in data-dependent acquisition mode (Xcalibur 4.5 software): full-scan MS (300–1800 m/z, 60,000 resolution) followed by 2 s data-dependent MS/MS (36% collision energy).

Mass spectra were searched against the mouse database using Sequest HT in Proteome Discoverer 2.5. Search criteria: full tryptic specificity, 1 missed cleavage, variable modification (oxidation [M]), fixed modifications (carbamidomethylation [C], TMT-6 plex [K-/N-terminal]), precursor ion tolerance (20 ppm MS, 0.02 Da MS/MS). Peptide FDR was calculated by Percolator ($q < 1\%$). Relative protein quantification was based on TMT reporter ion intensity, limited to proteins with ≥2 unique peptides. Protein ratios were calculated using median peptide ratios, with precision reflected by ratio variability.

Mass specrometry data analysis.

Protein isoforms were considered distinct in proteomic analysis. Phosphoproteomic analysis included unique and composite phosphopeptides (≥2 phosphorylation sites). Standardized abundance data were summed to generate unique protein/phosphopeptide IDs with aggregated values, scaled to an average sample abundance of 1. Data from different experiments were integrated by unique sample ID for comparison (e.g., SD6/S6 WT). Log_2 fold-change values were calculated using group means, with statistical significance assessed by multiple unpaired t-tests. Thresholds: proteomic analysis ($P < 0.01$, $|log_2$ fold-change$| > 0.3$); phosphoproteomic analysis of N1467D mice ($P < 0.05$, 75th percentile of log_2 fold-change). Datasets are listed in Supplementary Tables 11–12.

Phosphorylation state change (ΔPs) was calculated as the sum of log_2 fold-change values of significantly altered phosphopeptides ($P < 0.05$, 75th percentile of log_2 fold-change) from all protein isoforms. $\Delta Ps = 0$ if no phosphopeptides exhibited significant change. Details are in Supplementary Table 12.

Statistical methods.

All experiments were performed with biological replicates and independently repeated ≥2

times for reliability. Mice were randomly assigned numbers and blindly grouped for EEG/EMG recording and data processing. Data are presented as mean ± s.e.m. or mean ± s.d. as indicated, with sample sizes in figure legends. Protein band intensity was quantified using ImageJ (NIH). Statistical analysis was performed with GraphPad Prism and Microsoft Excel. Two-way ANOVA was used with Sidak's test (multiple means) or Fisher's LSD test (pairwise comparisons). Unpaired/paired two-tailed t-tests were used for independent/within-subject comparisons. Ordinary/repeated-measures one-way ANOVA with Fisher's LSD was applied for multiple group comparisons. Two-way ANOVA with Sidak's/Dunnett's/Fisher's LSD was used for two independent variables. Fisher's LSD was applied only if omnibus ANOVA indicated significance. Complete sample sizes, methods, and results are in figure legends and Supplementary Table 14. All raw data and code used in this study are available from the corresponding authors upon reasonable request.

Reference

1 Vyazovskiy, V. V. & Harris, K. D. Sleep and the single neuron: the role of global slow oscillations in individual cell rest. *Nat Rev Neurosci* **14**, 443-451 (2013).

2 Tononi, G. & Cirelli, C. Sleep and the price of plasticity: from synaptic and cellular homeostasis to memory consolidation and integration. *Neuron* **81**, 12-34 (2014).

3 Borbely, A. A., Daan, S., Wirz-Justice, A. & Deboer, T. The two-process model of sleep regulation: a reappraisal. *J. Sleep Res.* **25**, 131-143 (2016).

4 Sang, D. et al. Prolonged sleep deprivation induces a cytokine-storm-like syndrome in mammals. *Cell* **186**, 5500-5516.e5521 (2023).

5 Ma, C. & Dan, Y. The how and why of sleep: Motor theory and catecholamine hypothesis. *Neuron* (2025).

6 Ma, J. et al. Sleep prevents brain phosphoproteome disruption to safeguard survival. *Cell Discov* **11** (2025).

7 Diering, G. H. et al. Homer1a drives homeostatic scaling-down of excitatory synapses during sleep. *Science* **355**, 511-515 (2017).

8 Lou, T. et al. Hyper-Activation of mPFC Underlies Specific Traumatic Stress-Induced Sleep-Wake EEG Disturbances. *Frontiers in neuroscience* **14**, 883 (2020).

9 Zhou, R. et al. A signalling pathway for transcriptional regulation of sleep amount in mice. *Nature* **612**, 519-527 (2022).

10 Kim, S. J. et al. Kinase signalling in excitatory neurons regulates sleep quantity and depth. *Nature* **612**, 512-518 (2022).

11 Rasmussen, E. S., Takahashi, J. S. & Green, C. B. Time to target the circadian clock for drug discovery. *Trends in biochemical sciences* **47**, 745-758 (2022).

12 Muehlan, C., Roch, C., Vaillant, C. & Dingemanse, J. The orexin story and orexin receptor antagonists for the treatment of insomnia. *Journal of Sleep Research* **32** (2023).

13 Chemelli, R. M. et al. Narcolepsy in orexin knockout mice: molecular genetics of sleep regulation. *Cell* **98**, 437-451 (1999).

14 Lin, L. et al. The sleep disorder canine narcolepsy is caused by a mutation in the hypocretin (orexin) receptor 2 gene. *Cell* **98**, 365-376 (1999).

15 Shaw, P. J., Cirelli, C., Greenspan, R. J. & Tononi, G. Correlates of sleep and waking in

Drosophila melanogaster. *Science* **287**, 1834-1837 (2000).

16 Hendricks, J. C. et al. A non-circadian role for cAMP signaling and CREB activity in Drosophila rest homeostasis. *Nat Neurosci* **4**, 1108-1115 (2001).

17 Tatsuki, F. et al. Involvement of Ca(2+)-Dependent Hyperpolarization in Sleep Duration in Mammals. *Neuron* **90**, 70-85 (2016).

18 Wang, G. D. et al. Somatic Genetics Analysis of Sleep in Adult Mice. *Journal of Neuroscience* **42**, 5617-5640 (2022).

19 Funato, H. et al. Forward-genetics analysis of sleep in randomly mutagenized mice. *Nature* **539**, 378-383 (2016).

20 Allada, R., Cirelli, C. & Sehgal, A. Molecular Mechanisms of Sleep Homeostasis in Flies and Mammals. *Cold Spring Harbor perspectives in biology* **9** (2017).

21 Jan, M., O'Hara, B. F. & Franken, P. Recent advances in understanding the genetics of sleep. *F1000Research* **9** (2020).

22 Shafer, O. T. 25 years of "Sleep genes". *Fly* **19** (2025).

23 Franken, P., Chollet, D. & Tafti, M. The homeostatic regulation of sleep need is under genetic control. *J. Neurosci.* **21**, 2610-2621 (2001).

24 Krone, L. B. et al. A role for the cortex in sleep-wake regulation. *Nat Neurosci* **24**, 1210-1215 (2021).

25 Wang, Z. et al. Quantitative phosphoproteomic analysis of the molecular substrates of sleep need. *Nature* **558**, 435-439 (2018).

26 Liu, S., Liu, Q., Tabuchi, M. & Wu, M. N. Sleep Drive Is Encoded by Neural Plastic Changes in a Dedicated Circuit. *Cell* **165**, 1347-1360 (2016).

27 Gay, S. M. et al. Developing forebrain synapses are uniquely vulnerable to sleep loss. *Proc Natl Acad Sci U S A* **121**, e2407533121 (2024).

28 Johnson, J. L. et al. An atlas of substrate specificities for the human serine/threonine kinome. *Nature* **613**, 759-766 (2023).

29 Wang, C. et al. GPS 5.0: An Update on the Prediction of Kinase-specific Phosphorylation Sites in Proteins. *Genomics, proteomics & bioinformatics* **18**, 72-80 (2020).

30 Guillaumin, M. C. C. et al. Deficient synaptic neurotransmission results in a persistent sleep-like cortical activity across vigilance states in mice. *Current Biology* **35**, 1716-1729

(2025).

31 Zhang, Y. et al. Voltage Gated Ion Channels and Sleep. *J Membrane Biol* **257**, 269-280 (2024).

32 Han, S. et al. Na1.1 channels are critical for intercellular communication in the suprachiasmatic nucleus and for normal circadian rhythms. *Proceedings of the National Academy of Sciences of the United States of America* **109**, E368-E377 (2012).

33 Sanchez, R. E. A. et al. Circadian regulation of sleep in a pre-clinical model of Dravet syndrome: dynamics of sleep stage and siesta re-entrainment. *Sleep* **42** (2019).

34 Hu, W. et al. Distinct contributions of Na(v)1.6 and Na(v)1.2 in action potential initiation and backpropagation. *Nat Neurosci* **12**, 996-1002 (2009).

35 Ma, Z. X. et al. Deficiency of autism-related gene in mice disrupts sleep patterns and circadian rhythms. *Neurobiology of Disease* **168** (2022).

36 Cantrell, A. R. et al. Molecular mechanism of convergent regulation of brain Na(+) channels by protein kinase C and protein kinase A anchored to AKAP-15. *Mol Cell Neurosci* **21**, 63-80 (2002).

37 Chen, Y. A., Yu, F. H., Surmeier, D. J., Scheuer, T. & Catterall, W. A. Neuromodulation of Na+ channel slow inactivation via cAMP-dependent protein kinase and protein kinase C. *Neuron* **49**, 409-420 (2006).

38 Planells-Cases, R. et al. Neuronal death and perinatal lethality in voltage-gated sodium channel α-deficient mice. *Biophysical journal* **78**, 2878-2891 (2000).

39 Spratt, P. W. E. et al. Paradoxical hyperexcitability from Na1.2 sodium channel loss in neocortical pyramidal cells. *Cell reports* **36** (2021).

40 Winters, B. D., Huang, Y. H., Dong, Y. & Krueger, J. M. Sleep loss alters synaptic and intrinsic neuronal properties in mouse prefrontal cortex. *Brain Research* **1420**, 1-7 (2011).

41 Wang, Y. et al. Isoform-selective disruption of AKAP-localized PKA using hydrocarbon stapled peptides. *ACS chemical biology* **9**, 635-642 (2014).

42 Müller, P., Draguhn, A. & Egorov, A. V. Persistent sodium currents in neurons: potential mechanisms and pharmacological blockers. *Pflug Arch Eur J Phy* **476**, 1445-1473 (2024).

43 Liu, Y., Qin, N., Reitz, T., Wang, Y. & Flores, C. M. Inhibition of the rat brain sodium channel Nav1.2 after prolonged exposure to gabapentin. *Epilepsy research* **70**, 263-268

(2006).

44 Ehlers, C. L., Sanchez-Alavez, M. & Wills, D. Effect of gabapentin on sleep and delta and theta EEG power in adult rats exposed to chronic intermittent ethanol vapor and protracted withdrawal during adolescence. *Psychopharmacology* **235**, 1783-1791 (2018).

45 Lo, H. S. et al. Treatment Effects of Gabapentin for Primary Insomnia. *Clin Neuropharmacol* **33**, 84-90 (2010).

46 Shen, Y. N., Li, W., Ma, M. & Jiang, W. H. Efficacy and Safety of Gabapentin in Improving Sleep Quality of Patients with Sensory Nervous System Diseases: A Meta-Analysis. *Altern Ther Health M* **29**, 380-385 (2023).

47 Susantitapong, K., Dilokpattanamongkol, P., Sutherasan, Y., Liamsombut, S. & Suthisisang, C. Effects of gabapentin on slow-wave sleep period in critically ill adult patients: A randomized controlled trial. *Cts-Clin Transl Sci* **17** (2024).

48 Bruning, F. et al. Sleep-wake cycles drive daily dynamics of synaptic phosphorylation. *Science* **366** (2019).

49 Rosse, C. et al. PKC and the control of localized signal dynamics. *Nat Rev Mol Cell Bio* **11**, 103-112 (2010).

50 Torres-Quesada, O., Mayrhofer, J. E. & Stefan, E. The many faces of compartmentalized PKA signalosomes. *Cellular signalling* **37**, 1-11 (2017).

51 Ferrell, J. E. Feedback loops and reciprocal regulation: recurring motifs in the systems biology of the cell cycle. *Curr Opin Cell Biol* **25**, 676-686 (2013).

52 Needham, E. J., Parker, B. L., Burykin, T., James, D. E. & Humphrey, S. J. Illuminating the dark phosphoproteome. *Science signaling* **12** (2019).

53 Diering, G. H. & Huganir, R. L. The AMPA Receptor Code of Synaptic Plasticity. *Neuron* **100**, 314-329 (2018).

54 Quintela-López, T., Shiina, H. & Attwell, D. Neuronal energy use and brain evolution. *Curr Biol* **32**, R650-r655 (2022).

55 Lee, H. M. et al. The period of the circadian oscillator is primarily determined by the balance between casein kinase 1 and protein phosphatase 1. *Proceedings of the National Academy of Sciences of the United States of America* **108**, 16451-16456 (2011).

56 Nakajima, M. et al. Reconstitution of circadian oscillation of cyanobacterial KaiC

phosphorylation in vitro. *Science* **308**, 414-415 (2005).

57 Liao, M. et al. The P-loop NTPase RUVBL2 is a conserved clock component across eukaryotes. *Nature* **642**, 165-173 (2025).

58 Asano, F. et al. SIK3-HDAC4 in the suprachiasmatic nucleus regulates the timing of arousal at the dark onset and circadian period in mice. *Proceedings of the National Academy of Sciences of the United States of America* **120** (2023).

59 Drevon, D., Fursa, S. R. & Malcolm, A. L. Intercoder Reliability and Validity of WebPlotDigitizer in Extracting Graphed Data. *Behavior modification* **41**, 323-339 (2017).

60 Miyoshi, C. et al. Methodology and theoretical basis of forward genetic screening for sleep/wakefulness in mice. *Proceedings of the National Academy of Sciences of the United States of America* **116**, 16062-16067 (2019).

61 Campbell, I. G. EEG recording and analysis for sleep research. *Current protocols in neuroscience* **Chapter 10**, Unit10 12 (2009).

62 Wang, G. F. et al. An optogenetics- and imaging-assisted simultaneous multiple patch-clamp recording system for decoding complex neural circuits. *Nat Protoc* **10** (2015).

63 Shi, Y. Y. & Wang, G. F. Protocol to study microcircuits in the medial entorhinal cortex in mice using multiple patch-clamp recordings and morphological reconstruction. *STAR protocols* **5** (2024).

64 Deverman, B. E. et al. Cre-dependent selection yields AAV variants for widespread gene transfer to the adult brain. *Nat Biotechnol* **34**, 204-209 (2016).

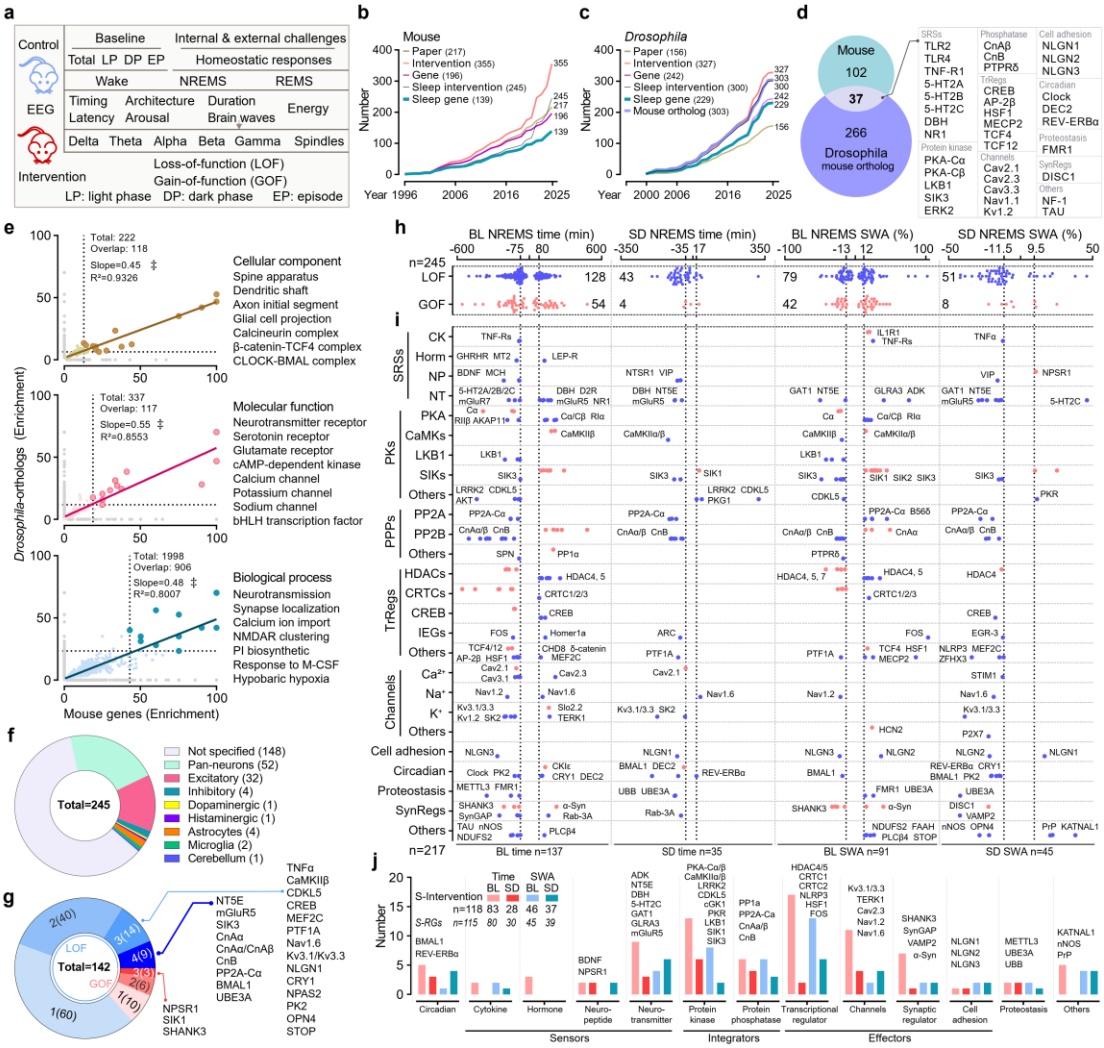

Fig. 1 Systematic identification and functional organization of sleep-regulatory genes.

a. Quantitative analysis of sleep parameters based on EEG/EMG.

b-e. Cumulative analysis of sleep studies in mice **(b)** and *Drosophila* **(c)**, overlap analysis **(d)**, and cross-species GO enrichment correlation analysis of their genes associated with sleep regulation **(e)**. ‡ $P < 0.001$.

f-g. Summary of cell-type-specific manipulations **(f)** and distribution of unique genetic manipulations across different sleep traits **(g)**.

h-i. Quantitative analysis of 245 genetic interventions on 4 NREMS traits **(h)** and mapping of interventions exceeding the 75th percentile to 26 functional classes **(i)**.

j. Functional distribution of unique S-Interventions, S-RGs and top 10 S-Interventions across 4 NREMS traits.

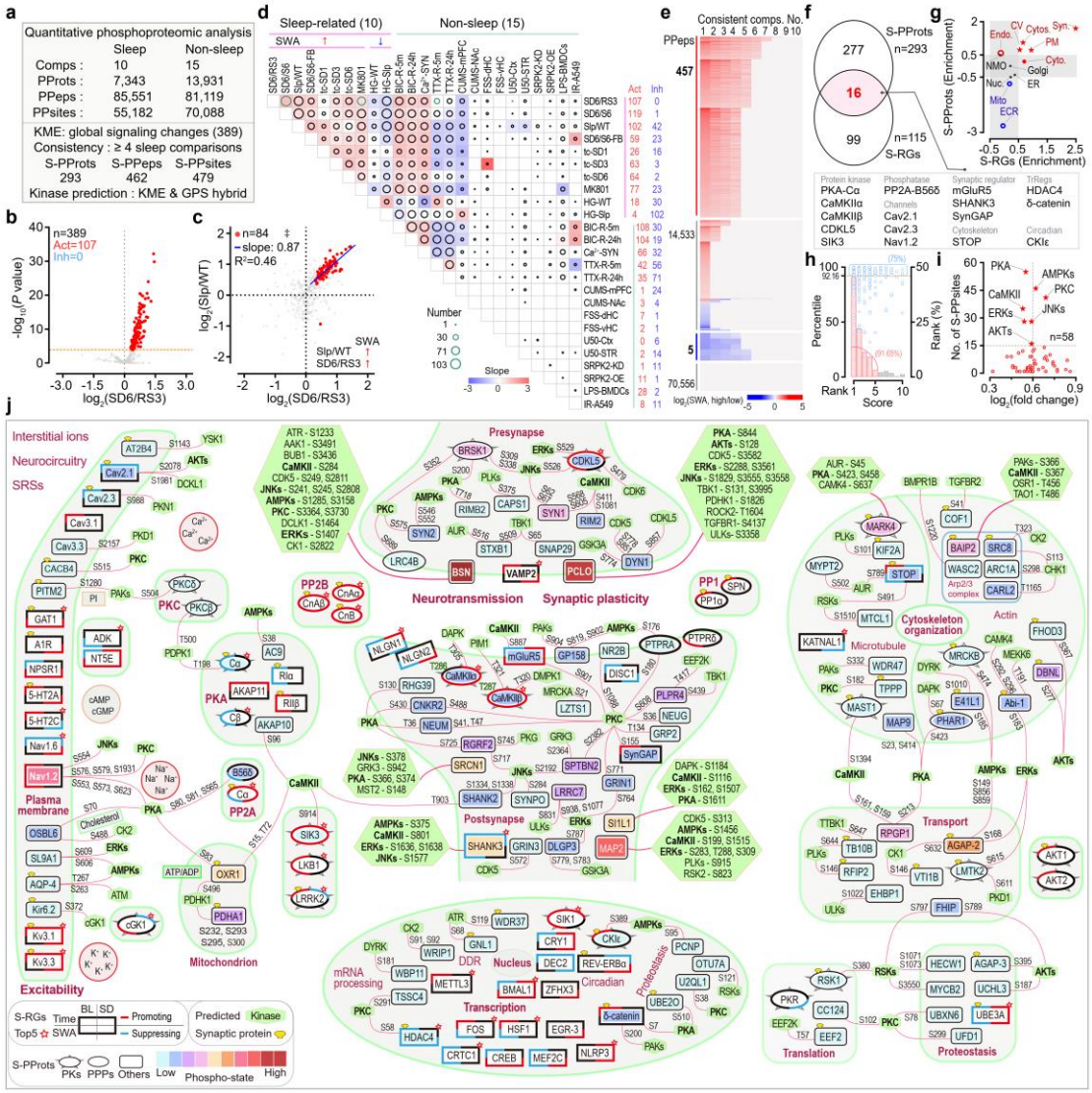

Fig. 2 Quantitative phosphoproteomic analysis defines the sleep-regulatory signaling network.

a. Overview of quantitative phosphoproteomic analysis.

b-d. KME analysis of the SD6/RS3 comparison **(b)**, correlation analysis of significantly altered kinase motifs between SD6/RS3 and Slp/WT comparisons **(c)**, and correlation matrix of 25 conditional datasets **(d)**. Act, activated; Inh, inhibited. ‡ $P < 0.001$.

e-g. Consistency analysis of phosphopeptides across 10 sleep-related datasets to define S-PPeps **(e)**, overlap analysis **(f)**, and slimmed GO enrichment analysis between S-RGs and S-PProts **(g)**.

h-i. Kinase prediction rank scores and percentile distribution for 479 S-PPsite-kinase pairs **(h)**, and annotated site distribution of 58 kinase families according to the mean $\log_2$(fold change) of S-PPsites per kinase family **(i)**.

j. Hierarchical functional architecture of sleep-regulatory components reveals core processes governing sleep homeostasis.

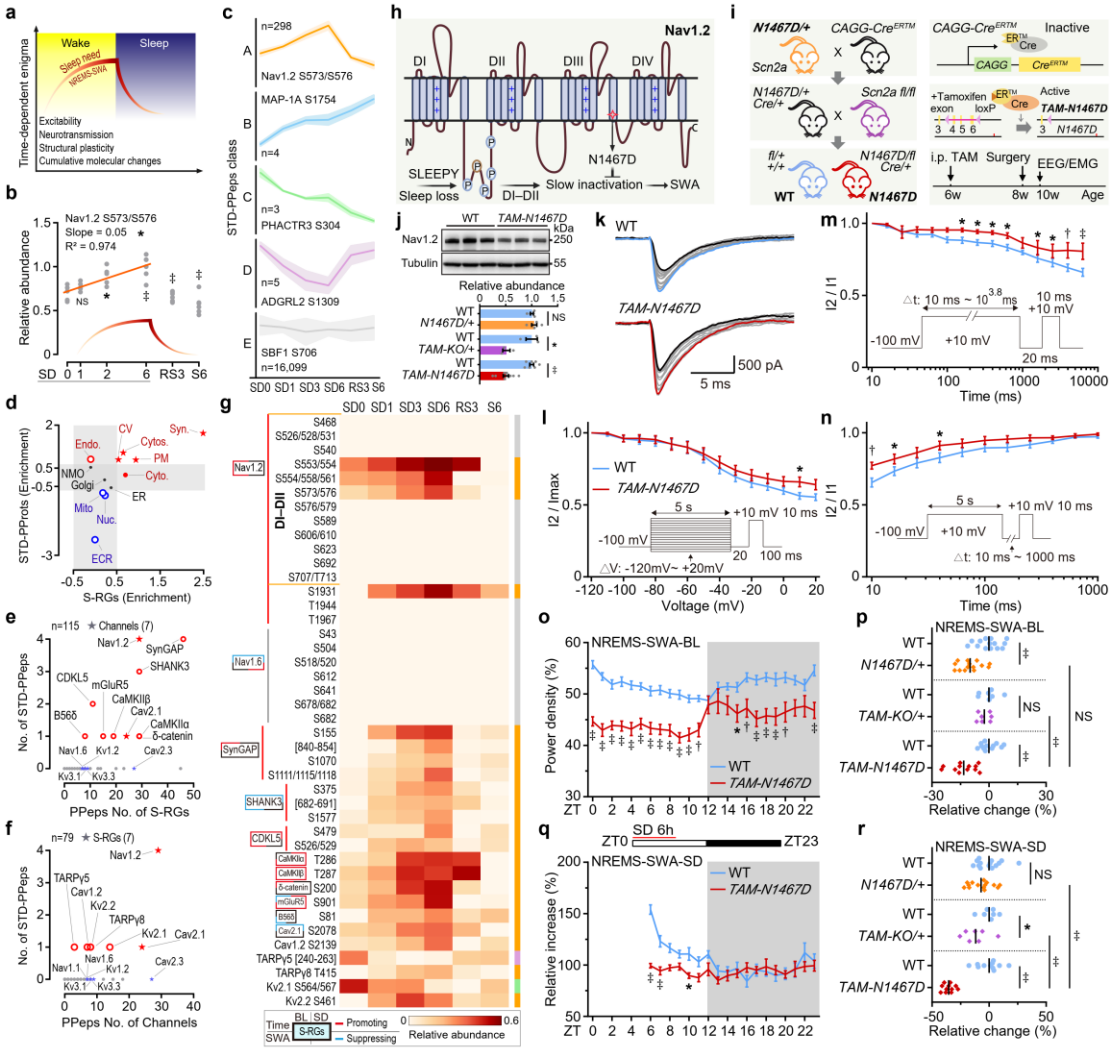

Fig. 3 Impaired slow inactivation of Nav1.2 attenuates NREMS-SWA.

a. Conceptual model of the time-dependent regulatory mechanism of sleep homeostasis.

b-d. Parallel analysis of temporal dynamics of phosphopeptides and NREMS-SWA changes **(b)**, examples of 5 classes of STD-PPeps **(c)**, and slimmed GO enrichment analysis between S-RGs and STD-PProts **(d)**.

e-g. Number of STD-PPeps in S-RGs **(e)**, ion channels **(f)**, and heatmap of representative PPeps **(g)**.

h-j. Schematic of the domain structure of Nav1.2 **(h)**, construction strategy for tamoxifen-induced *Scn2a*^{N1467D} homozygous mice (*TAM-N1467D*) **(i)**, and immunoblots (top) with quantitative analysis (bottom) of brain Nav1.2 abundance **(j)**. WT vs. *N1467D/+* (n=5 each), *TAM-KO/+* (n=3 each), *TAM-N1467D* (n=7 vs. 9).

k-n. Measurements of slow inactivation in layer 5 pyramidal neurons from WT and *TAM-N1467D* mice: representative current traces **(k,** 15 vs. 15**)**, voltage dependence **(l**, 17 vs. 16**)**, onset **(m**, 10 vs. 7**)**, and recovery **(n**, 17 vs. 9**)**, voltage protocols are shown in insets.

o-r. Analysis of baseline **(o, p)** and rebound **(q, r)** NREMS-SWA. WT vs. *N1467D/+* (n=14

each), *TAM-KO/+* (n=7 each), *TAM-N1467D* (n=12 each).

Data: mean ± s.e.m. Two-tailed *t*-test (**j**); Two-way ANOVA (Fisher's LSD: **l-n**; Sidak's: **o, q**); Ordinary one-way ANOVA (Fisher's LSD: **p, r**).

*$P < 0.05$. †$P < 0.01$. ‡$P < 0.001$. NS, not significant ($P > 0.05$).

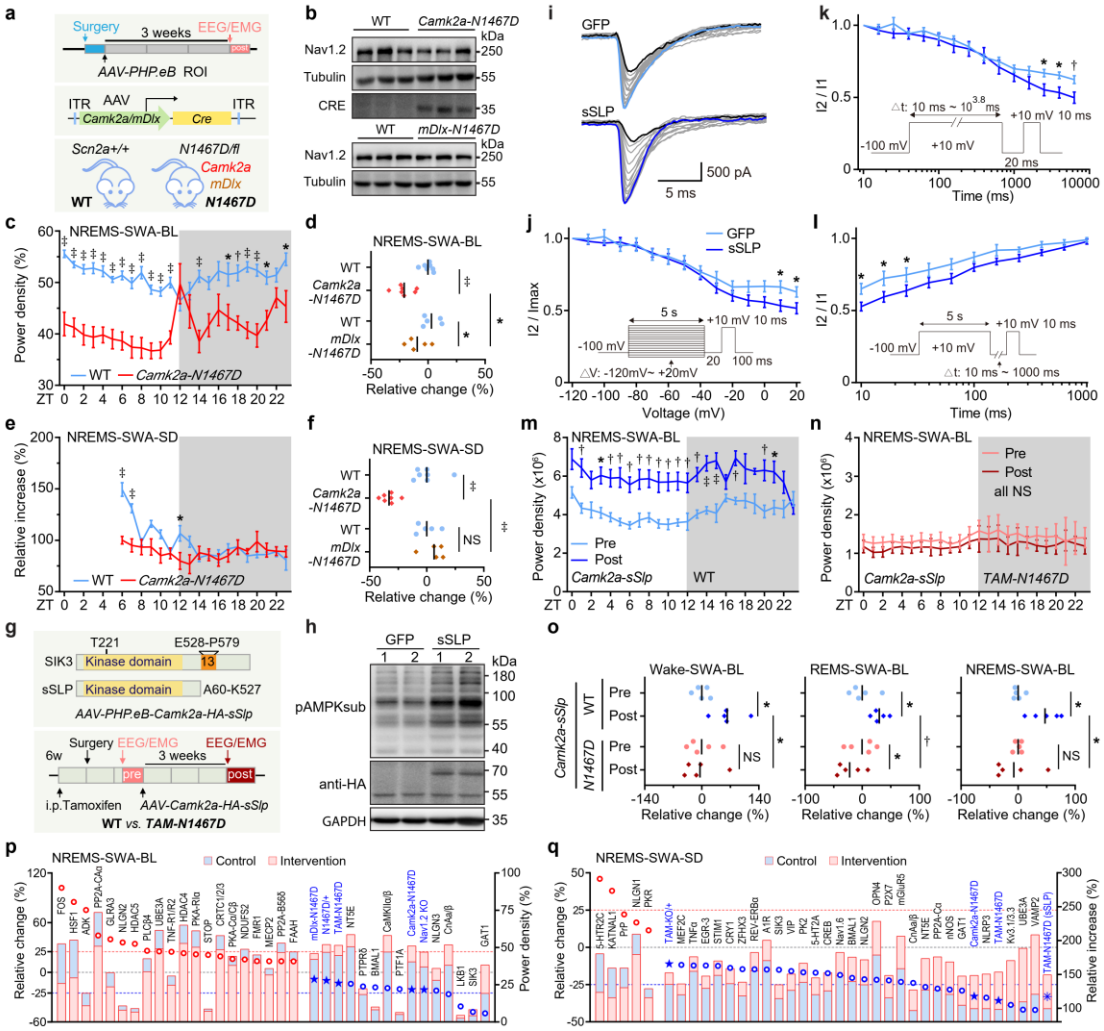

Fig. 4 Nav1.2 acts downstream of SLEEPY kinase in excitatory neurons.

a-f. Schematic of conditional knockout of *Scn2a* **(a)**, immunoblot of brain Nav1.2 abundance **(b)**, and analysis of baseline **(c, d)** and rebound NREMS-SWA **(e, f).** WT *vs.* *Camk2a-N1467D* (n=7 each), *mDlx-N1467D* (n=5 each).

g-l. Schematic of the truncated SIK3 protein (sSLP) structure and experimental design for sleep analysis **(g)**. Immunoblot of the AMPK substrate motif (pAMPKsub) in brain lysates **(h)**, and measurements of slow inactivation in layer 5 pyramidal neurons from mice expressing GFP or sSLP. Representative current traces (**i**, 15 vs. 15), voltage dependence (**j**, 38 vs. 25), onset (**k**, 33 vs. 26), and recovery (**l**, 33 vs. 18).

m-o. Circadian **(m, n)** and quantitative **(o)** analyses of baseline SWA before (pre) and after (post) AAV-*Camk2a-HA-sSlp* injection. WT *vs.* *TAM-N1467D* (n=5 each).

p-q. Relative comparison of loss-of-function strains of S-RGs and Nav1.2 slow inactivation-deficient strains for NREMS-SWA **(p)** and SD-induced NREMS-SWA rebound **(q).**

Data: mean ± s.e.m. Two-way ANOVA (Sidak's: **c, e, m, n**; Fisher's LSD: **j-l**); Ordinary one-way ANOVA (Fisher's LSD: **d, f**); Two-tailed *t*-test (**o**).

1230 *$P < 0.05$. †$P < 0.01$. ‡$P < 0.001$. NS, not significant ($P > 0.05$).

1231

1232

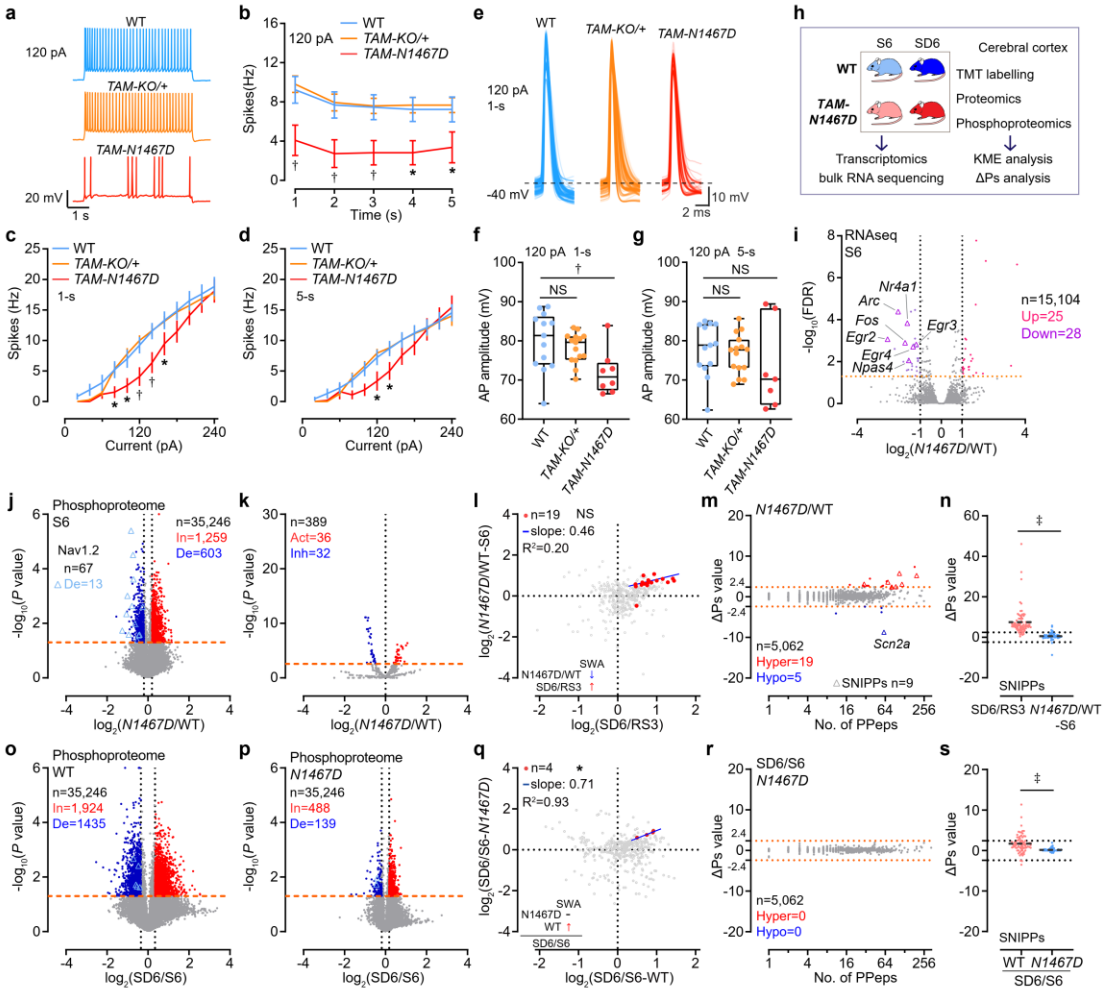

Fig. 5 Nav1.2 alters neuronal excitability and functions as a homeostatic sleep effector.

a-g. Evoked responses to a 5-s depolarizing current step at 120 pA **(a)**, spike counts per second **(b)**, and spike counts during the 1-s **(c)** and 5-s **(d)** epoch (20–240 pA). AP waveforms **(e)** and AP amplitude quantified during the 1-s **(f)** and 5-s **(g)** epochs at 120 pA. WT (n = 13), *TAM-KO/+*(n = 15), *TAM-N1467D* (n = 11).

h-i. Multi-omics analysis design for *TAM-N1467D* mice **(h)**, and RNA expression volcano plot of the N1467D/WT (S6) comparison **(i)**, IEGs are labeled.

j-n. Phosphoproteomic analysis of the N1467D/WT (S6) comparison: phosphopeptide changes **(j)**, kinase motif enrichment **(k)**, correlation of significantly altered kinases with SD6/RS3 **(l)**, global **(m)** and quantified ΔPs analysis **(n)**.

o-s. Phosphoproteomic analysis of SD6/S6-WT and SD6/S6-N1467D comparisons: phosphopeptide changes **(o, p)**, correlation of significantly altered kinases **(q)**, global **(r)** and quantified ΔPs analysis **(s)**.

Data: mean ± s.e.m. Two-way ANOVA (Fisher's LSD: **b-d)**; Ordinary one-way ANOVA (Fisher's LSD: **f, g**); Two-tailed *t*-test **(n, s)**.

Up, up-regulated; Down, down-regulated; In, increase; De, decrease; Act, activated; Inh,

inhibited. Hyper, hyperphosphorylated; Hypo, hypophosphorylated.

*$P < 0.05$. †$P < 0.01$. ‡$P < 0.001$. NS, not significant ($P > 0.05$).

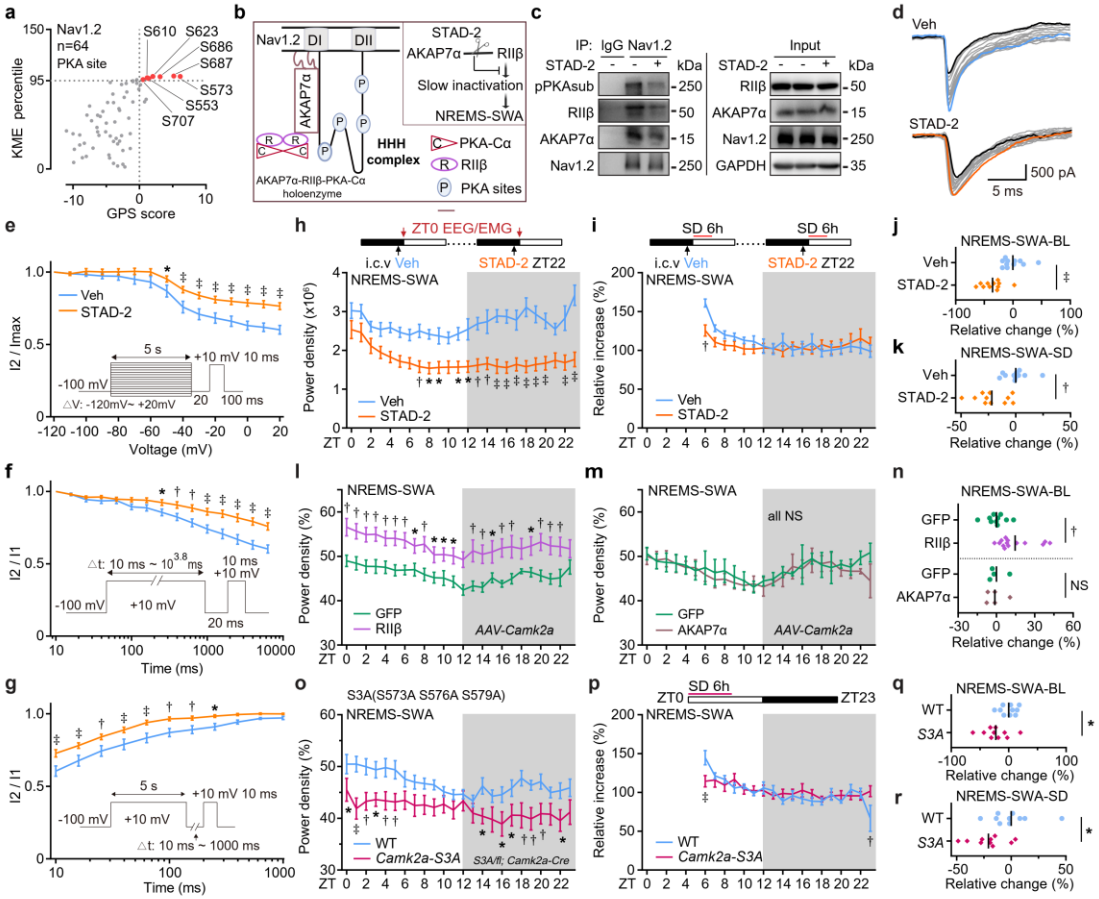

Fig. 6 The RIIβ-PKA holoenzyme promotes Nav1.2 phosphorylation and sleep quality.

a. Prediction of PKA substrate sites in Nav1.2 (n=64).

b. Schematic of AKAP7α-RIIβ-PKA-Cα-Nav1.2 DI–II loop interaction and STAD-2 effect.

c-g. Nav1.2 Co-IP after STAD-2 treatment **(c)**, slow inactivation of layer 5 pyramidal neurons (Veh vs. STAD-2): traces (**d**, 15 vs. 15), voltage dependence (**e**, 16 vs. 30), onset (**f**, 13 vs. 26), and recovery (**g**, 16 vs. 23).

h-k. Baseline **(h, j)** and rebound NREMS-SWA **(i, k)** in Veh- or STAD-2-injected mice (n=11).

l-n. Circadian **(l, m)** and quantitative **(n)** analyses of baseline NREMS-SWA. GFP vs. RIIβ (10 vs. 14); GFP vs. AKAP7α (4 vs. 5).

o-r. Baseline **(o, q)** and rebound NREMS-SWA **(p, r)** in *Camk2a-S3A* mice. WT *vs.* *Camk2a-S3A* (n=10 each).

Data: mean ± s.e.m. Two-way ANOVA (Fisher's LSD: **e-g, l, m, o, p**; Sidak's: **h, i**); Two-tailed *t*-test (**j, k, n, q, r**).

* $P < 0.05$; † $P < 0.01$; ‡ $P < 0.001$; NS, not significant, $P > 0.05$.

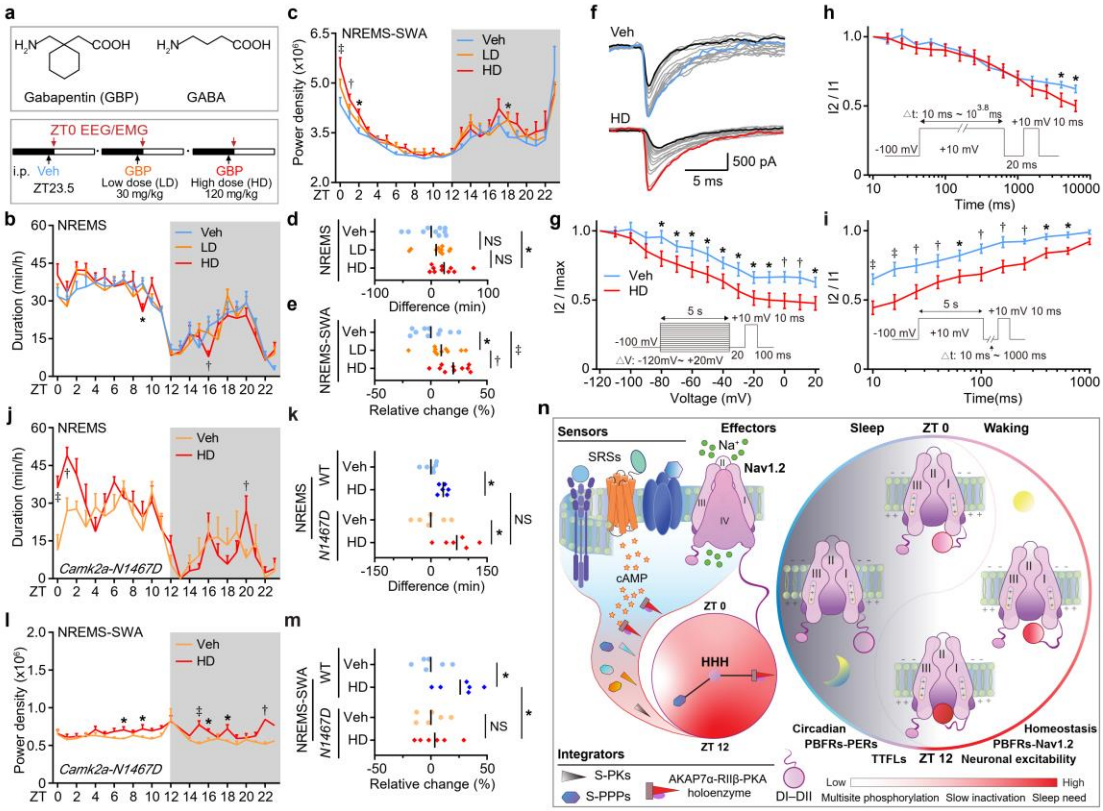

Fig. 7 Gabapentin improves sleep quality *via* Nav1.2 in mice.

a. Chemical structure of gabapentin (GBP) and experimental protocol.

b-i. Circadian analysis of baseline NREMS time **(b, d)** and NREMS-SWA **(c, e)** in mice i.p. injected with Veh or GBP (n=10); slow inactivation of layer 5 pyramidal neurons (Veh vs. HD-GBP): traces (**f**, 15 vs. 15), voltage dependence (**g**, 38 vs. 29), onset (**h**, 33 vs. 21), and recovery (**i**, 33 vs. 17).

j-m. Circadian and quantitative analyses of baseline NREMS **(j, k)** and NREMS-SWA **(l, m)** in WT and *Camk2a-N1467D* mice injected with Veh and HD-GBP (n=6 each).

n. Molecular model: the AKAP7α-RIIβ-PKA-Cα-Nav1.2 complex forms a compact homeostatic module that links upstream signaling to sleep quality control.

Data: mean ± s.e.m. Ordinary one-way ANOVA (Fisher's LSD: **d, e**); Two-way ANOVA (Fisher's LSD: **b, c, g-j, l**); Wilcoxon matched-pairs test and Mann-Whitney test **(k, m)**.

* $P < 0.05$; † $P < 0.01$; ‡ $P < 0.001$; NS, not significant, $P > 0.05$.

a

Cellular component	Shared	Mouse specific	Mouse orthologs specific
GO:0098666 Serotonin receptor	Htr2a; Htr2b; Htr2c		
GO:0070369 Beta-catenin-TCF7 complex	Tcf4; Tcf7l2		
GO:1990513 CLOCK-BMAL complex	Clock; Npas2;	Bmal1;	Bmal2
GO:0005955 Calcineurin complex	Ppp3ca; Ppp3cb; Ppp3r1		
GO:0071664 Catenin-TCF7 complex	Tcf4; Tcf7l2		
GO:0097444 Spine apparatus	Fmr1;	Ppp1r9b; Chrna7;	Ppfia1
GO:0001518 VGSC channel complex	Cacna1i; Scn1a;	Cacna1g; Scn2a; Scn8a;	Cacna1h
GO:0030673 Axolemma	Mapt;	Adora1; Kcnc1; Kcnc2; Kcnc3; Chrna7;	Slc1a2
GO:0043198 Dendritic shaft	Nlgn1;	Grm5; Grm7; Hcn2; Homer1; Htr2a;	Nlgn2; Asic1; Cacna1b; Cacna1c; Chrna7; Drd1; Epha4; Hspa5; Htr2a; Negr1; Ntsr1; Prkar2b; Slc1a2; Syngap1
GO:0043194 Axon initial segment	Kcna2; Scn1a;	Scn2a; Scn8a;	Kcnab2; Nfasc; Nrcam
GO:0044305 Calyx of Held	Cacna1a; Kcna2;	Adora1; Kcnc1; Kcnk2; Kcnc3;	Nos1; Glra1; Kcna3
GO:0005891 VGCC channel complex	Cacna1a; Cacna1e; Cacna1i;	Cacna1g;	Cacna1b; Cacna1c; Cacna1d; Cacna1h; Cacna1s; Pde4b
GO:0097386 Glial cell projection	Fmr1; Mapt;	Grm5; Kcnk2;	App; Grm2; Grm3; Nfasc; Slc1a2
GO:0044304 Main axon	Dbh; Kcna2; Mapt; Scn1a;	Adora1; Crh; Kcnc1; Kcnc2; Kcnc3; Kcnk2; Scn2a; Scn8a; Tnfrsf1b;	App; Chrna7; Kcnab1; Kcnab2; Nfasc; Nrcam; Slc1a2
GO:0043195 Terminal bouton	Dbh; Fmr1; Grin1;	Adora1; Bdnf; Gabrb3; Grm7; Kcnc2; Lrrk2; Ntsr1; P2rx7; Ppp2ca; Pmp; Rab3a; Snca;	Cyfip1; Erc2; Slc18a1; Slc18a2; Slc18a3; Slc1a7

b

Molecular function	Shared	Mouse specific	Mouse orthologs specific
GO:0071886 DOI binding	Htr2a; Htr2c		
GO:0001587 Serotonin receptor activity	Htr2a; Htr2b; Htr2c		
GO:0004691 PKA activity	Prkaca; Prkacb		
GO:0008332 Low VGCC activity	Cacna1i;	Cacna1g;	Cacna1h
GO:0004690 cNMP-dependent PK activity	Prkaca; Prkacb;	Prkg1	
GO:0051378 Serotonin binding	Htr2a; Htr2b; Htr2c;	Htr1a; Htr4;	Slc6a4;
GO:0099511 VGCC cytosolic	Cacna1a; Cacna1e;	Cacna1b;	Cacna1d
GO:0099626 VGCC presynaptic	Cacna1a; Cacna1e;	Cacna1b;	Cacna1d
GO:0004993 Serotonin receptor activity	Htr2a; Htr2b; Htr2c;	Htr1a;	Htr4
GO:0043176 Amine binding	Htr2a; Htr2b; Htr2c;	Adrb1;	Hrh3; Htr1a; Htr4; Slc6a3; Slc6a4
GO:0099589 Serotonin receptor activity	Htr2a; Htr2b; Htr2c;	Htr1a;	Htr4;
GO:0015271 Outward rectifier Kv activity	Kcna2;	Kcnk2; Kcnk9; Kcnt1;	Kcna3; Kcnb1; Kcnd3; Kcnk5; Kcnk10; Kcnk18
GO:0061809 NAD+ nucleosidase activity	Tlr2; Tlr4;	Il1r1; Tlr1;	Tlr6
GO:0030594 Neurotransmitter receptor activity	Grin1; Htr2a; Htr2b; Htr2c;	Adrb1; Drd2; Gabrb1; Gabrb3; Glra3; Grm1; Grm5; Hrh3; Chrna2; Chrna3; Chrna4; Chrna6; Chrna7; Chrnd; Drd1; Drd5; Gabrd; Gabrp; Gabrr1; Gabrr2; Gabrr3; Glra1; Glra2; Glra4; Glrb; Grin2c; Htr1a;	Htr4;
GO:0005251 Delayed rectifier Kv activity	Kcna2;	Kcnc1; Kcnc2;	Kcnc3; Kcna3; Kcnb1; Kcnb2

c

Biological process	Shared	Mouse specific	Mouse orthologs specific
GO:1903974 Response to M-CSF stimulus	Tlr2; Tlr4		
GO:0010513 PI biosynthetic process	Htr2a; Htr2b; Htr2c		
GO:1903971 Response to M-CSF	Tlr2; Tlr4		
GO:1902474 Protein localization to synapse	Mapt; Nlgn1; Nlgn3;	Nlgn2	
GO:1990910 Response to hypobaric hypoxia	Creb1; Hsf1;	Dnm1l	
GO:0010511 PI biosynthetic process	Htr2a; Htr2b; Htr2c		
GO:0046960 Sensitization	Htr2a; Htr2c;	Drd1; Drd5	
GO:0003332 ECM constituent secretion	Tnfrsf1a;	Tnfrsf1b;	Notch1
GO:1904466 Matrix metallopeptidase secretion	Tlr2; Tlr4		
GO:1900034 Cellular response to heat	Mapt; Hsf1		
GO:0097114 NMDAR clustering	Nlgn1;	Shank3;	Apoe; Htr1a
GO:1905949 Calcium ion import	Ppp3cb; Ppp3r1;	Ppp3ca	
GO:0014056 ACH secretion, neurotransmission	Cacna1a; Htr2c; Slc18a3;	Chrna3	
GO:1901610 Vesicle transport	Stk11; Mecp2		
GO:0097104 PSD membrane assembly	Nlgn1; Nlgn2; Nlgn3;	Ephb2;	Nrxn2

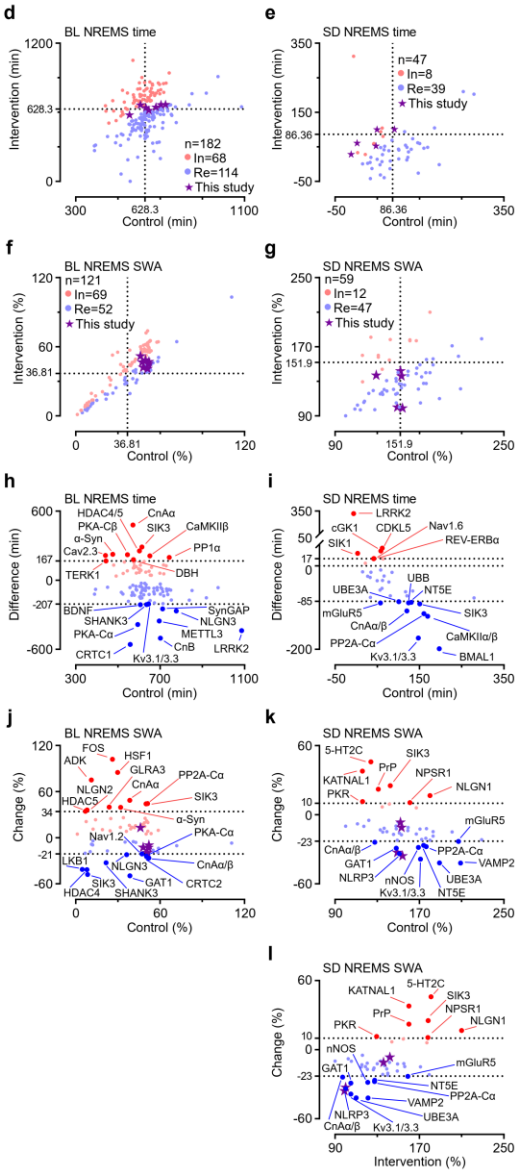

Extended Data Fig. 1 Overview of sleep genetic studies on mice and *Drosophila*.

a-c. GO enrichment analysis of cellular component **(a)**, molecular function **(b)**, and biological process **(c)** for shared, mouse-specific, and mouse-ortholog–specific genes.

d-g. Scatter plots of measured intervention and control values for baseline NREMS duration **(d)**, SD-induced NREMS duration **(e)**, baseline NREMS-SWA **(f)**, and SD-induced NREMS-SWA rebound **(g)**.

h-l. Scatter plots illustrating intervention-associated changes in baseline NREMS duration **(h)**, SD-induced NREMS duration **(i)**, baseline NREMS-SWA **(j)**, and SD-induced NREMS-SWA rebound **(k)** plotted against control values. SD-induced NREMS-SWA rebound is additionally plotted against intervention values **(l)**.

Red, intervention > control. blue, intervention < control. Asterisks: present study.

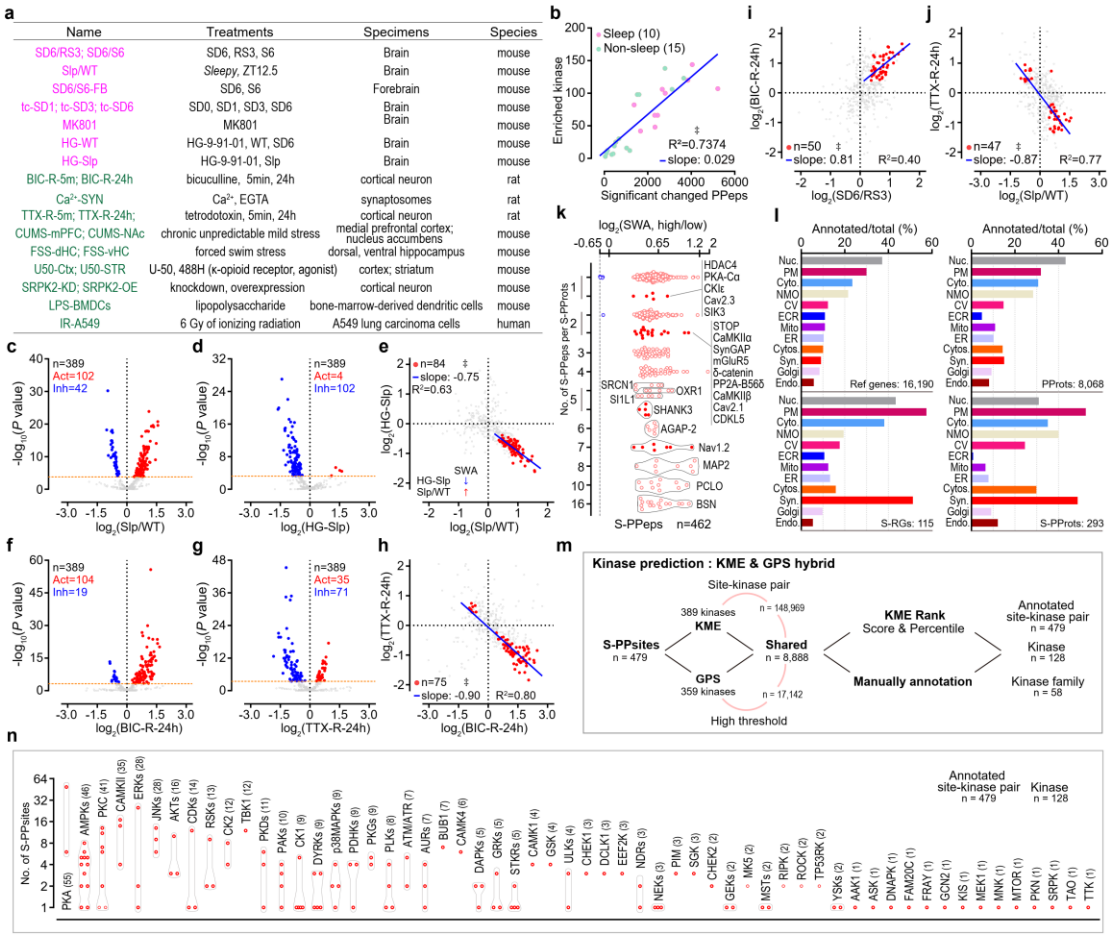

Extended Data Fig. 2 Summary of quantitative phosphoproteomic datasets.

a-b. Details **(a)** and correlation analysis **(b)** of significantly altered phosphopeptides and enriched kinase motifs of 25 collected phosphoproteomic datasets.

c-j. Global kinase motif enrichment for Slp/WT **(c)**, Slp/HG **(d)**, BIC-R-24h **(f)**, and TTX-R-24h **(g)**, and correlation analysis for Slp/WT *vs.* Slp/HG **(e)**, BIC-R-24h *vs.* TTX-R-24h **(h)**, SD6/RS3 *vs.* BIC-R-24h **(i)**, and Slp/WT *vs.* TTX-R-24h **(j)**.

k. S-PPeps distribution ordered by their count in S-PProts and mean $\log_2$(fold change), filled red circles: S-RGs.

l. Subcellular localization of the indicated gene groups.

m. Site–kinase prediction workflow using the hybrid KME–GPS method.

n. Distribution of 479 annotated site–kinase pairs across 128 individual kinases.

‡ $P < 0.001$.

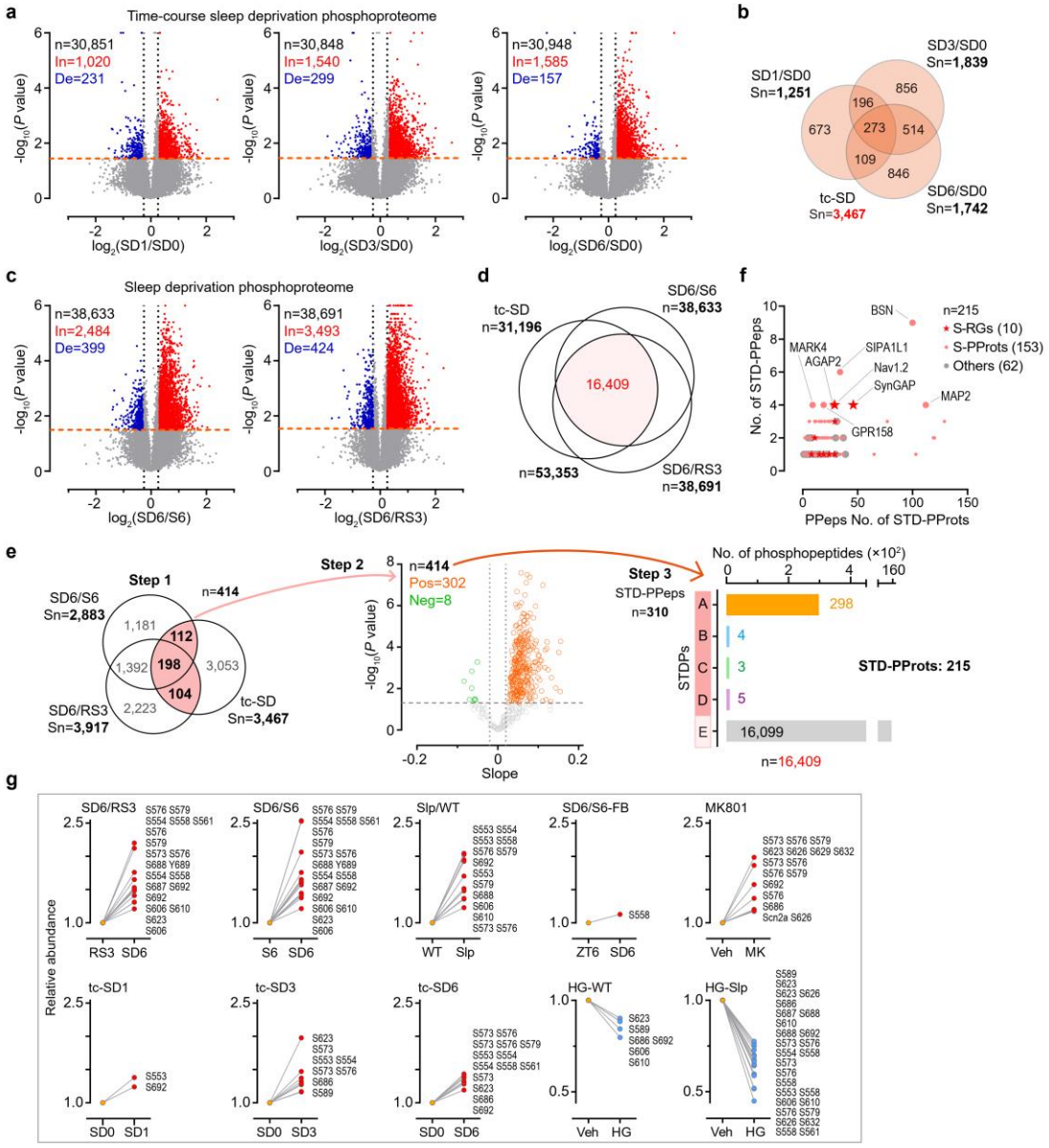

Extended Data Fig. 3 Classification approach for sleep time-dependent phosphopeptides.

a-b. Phosphoproteomic analysis of tc-SD **(a)** and overlap analysis of tc-SD-derived phosphopeptides **(b)**.

c-d. Phosphoproteomic analysis of SD6/S6 and SD6/RS3 **(c)** and overlap analysis of phosphopeptides across SD models **(d)**.

e. Analysis approach for the classification of STD-PPeps.

f. Scatter plot of STD-PPeps number in 215 STD-PProts.

g. Relative abundance of Nav1.2 DI-DII loop phosphopeptides across 10 sleep-related comparisons.

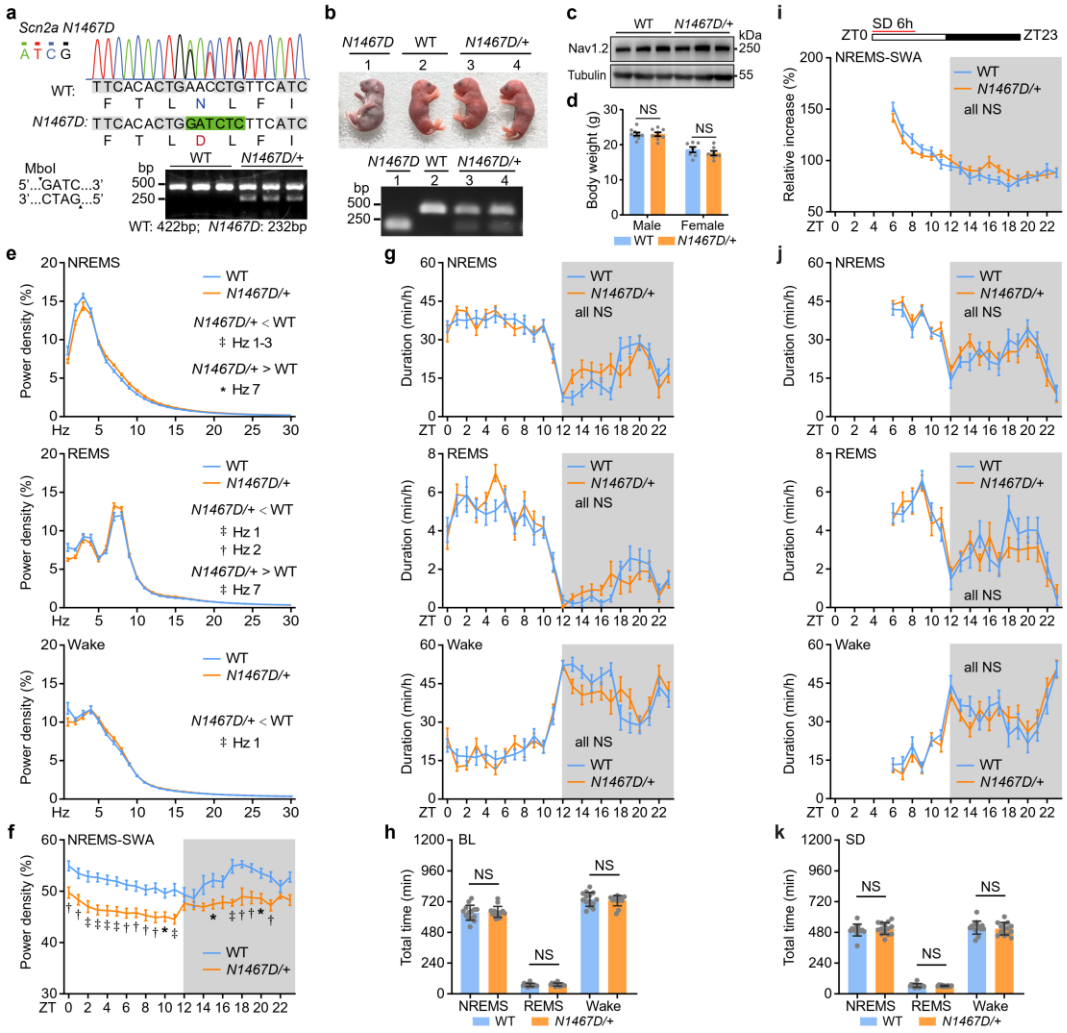

Extended Data Fig. 4 Generation and characterization of *Scn2a*^{N1467D} mutant mice.

a-b. Direct sequencing, genotyping design, and RT-PCR of the *N1467D/+* mutant mouse **(a)**, and postnatal mortality of *N1467D* mice **(b)**.

c-d. Immunoblot of brain Nav1.2 abundance **(c)**, and body weight comparison between WT (n=9 male, 7 female) and *N1467D/+* (n= 8 male, 7 female) mice **(d)**.

e-k. Sleep analysis of WT *vs.* *N1467D/+* (n=14 each) mice. Relative EEG power spectrum **(e)**; baseline NREMS-SWA **(f)**, hourly **(g)** and total **(h)** duration of NREMS, REMS, and wakefulness; rebound NREMS-SWA **(i)**, hourly **(j)** and total **(k)** duration of NREMS, REMS, and wakefulness after 6 h SD.

Data: mean ± s.e.m. (**e-g, i, j**); mean ± s.d. (**d, h, k**). Two-way ANOVA (Sidak's test: **e-g, i, j**); Two-tailed *t*-test (**d, h, k**).

* $P < 0.05$; † $P < 0.01$; ‡ $P < 0.001$; NS, not significant, $P > 0.05$.

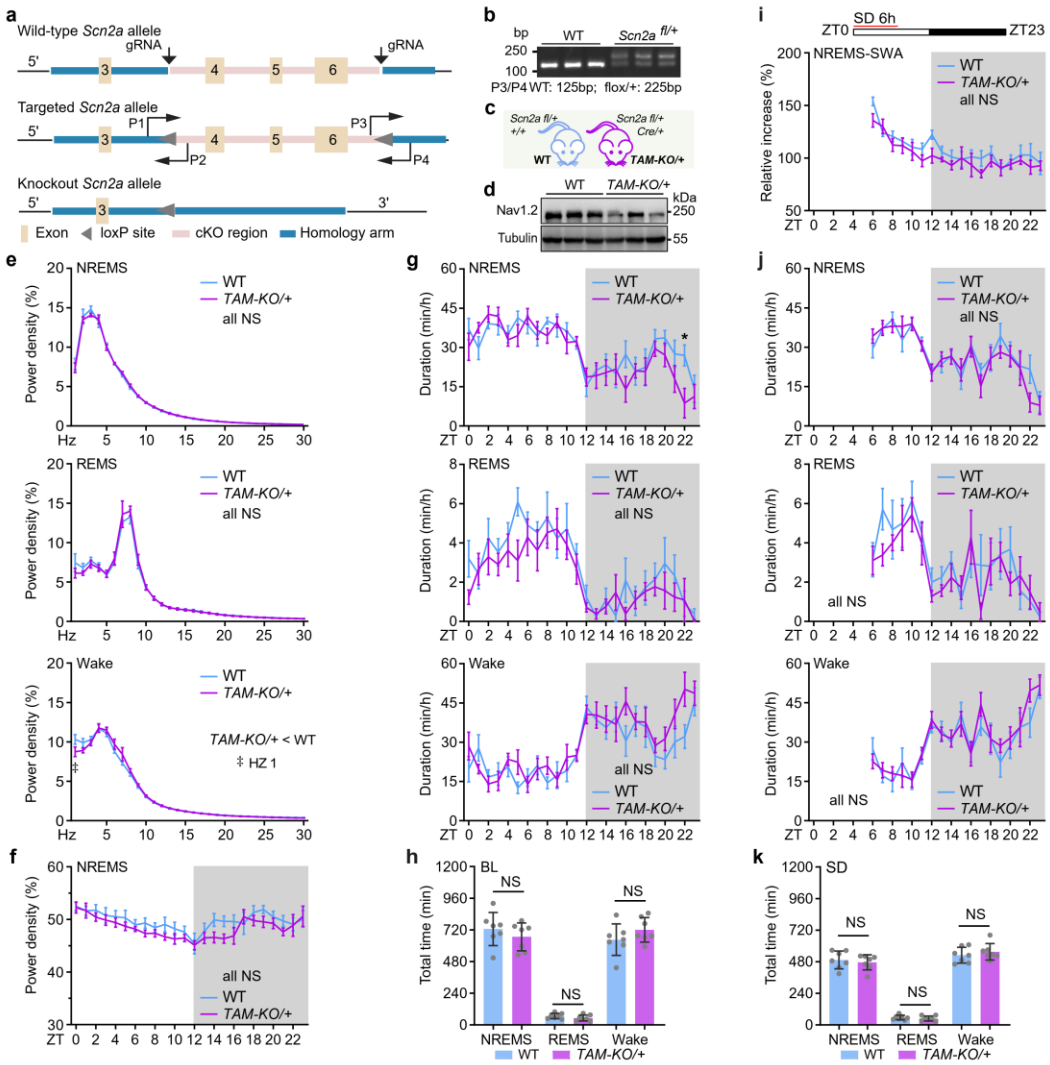

Extended Data Fig. 5 Sleep analysis of *TAM-KO/+* mice.

a-d. Gene editing schematic **(a)**, genotyping **(b)**, breeding strategy **(c)**, and immunoblot of brain Nav1.2 abundance **(d)**.

e-k. Sleep analysis of WT and *TAM-KO/+* (n=7 each) mice. Relative EEG power spectrum **(e)**, baseline NREMS-SWA **(f)**, hourly **(g)** and total **(h)** duration of NREMS, REMS, and wakefulness; rebound NREMS-SWA **(i)**, hourly **(j)** and total **(k)** duration of NREMS, REMS, and wakefulness after 6 h SD.

Data: mean ± s.e.m. (**e-g, i, j**); mean ± s.d. (**h, k**). Two-way ANOVA (Sidak's: **e-g, i, j**); Two-tailed *t*-test (**h, k**).

* $P < 0.05$; † $P < 0.01$; ‡ $P < 0.001$; NS, not significant, $P > 0.05$.

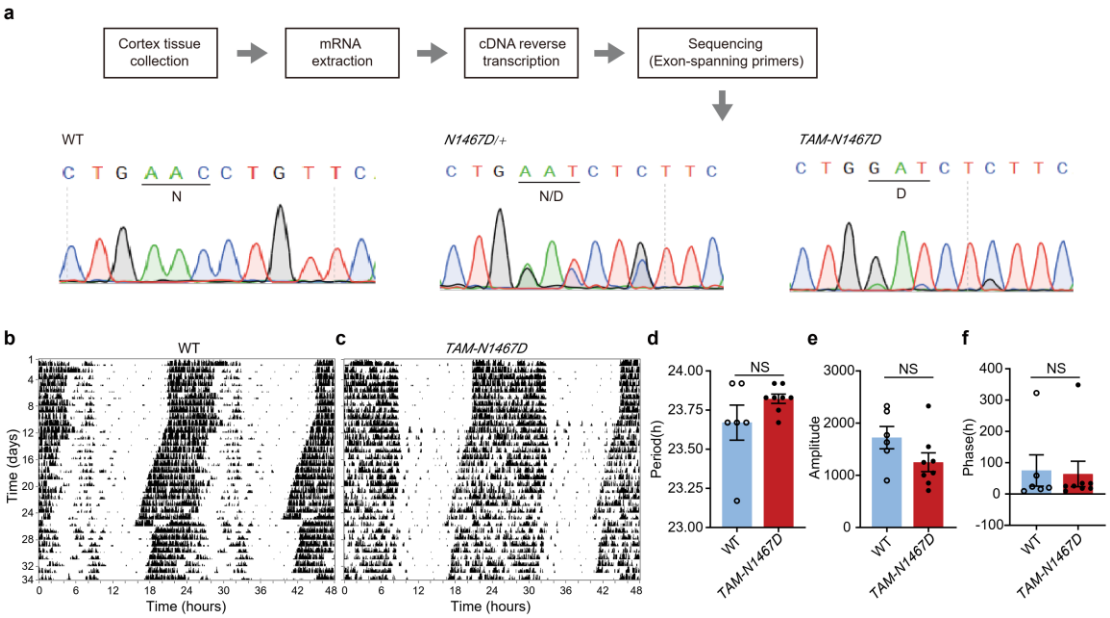

Extended Data Fig. 6 Circadian rhythm analysis of *TAM-N1467D* mice.

a. Sanger sequencing confirmation of the N1467D mutation in cortical mRNA isolated from *TAM-N1467D* mice.

b-c. Representative actograms of circadian wheel-running activity in WT **(b)** and *TAM-N1467D* **(c)** mice.

d-f. Quantification of circadian period **(d)**, rhythm amplitude **(e)**, and phase **(f)** in WT(n=6) and *TAM-N1467D* (n=8) mice.

Data: mean ± s.e.m. (**d, e, f**). Two-tailed *t*-test (**d, e, f**).

NS, not significant, $P > 0.05$.

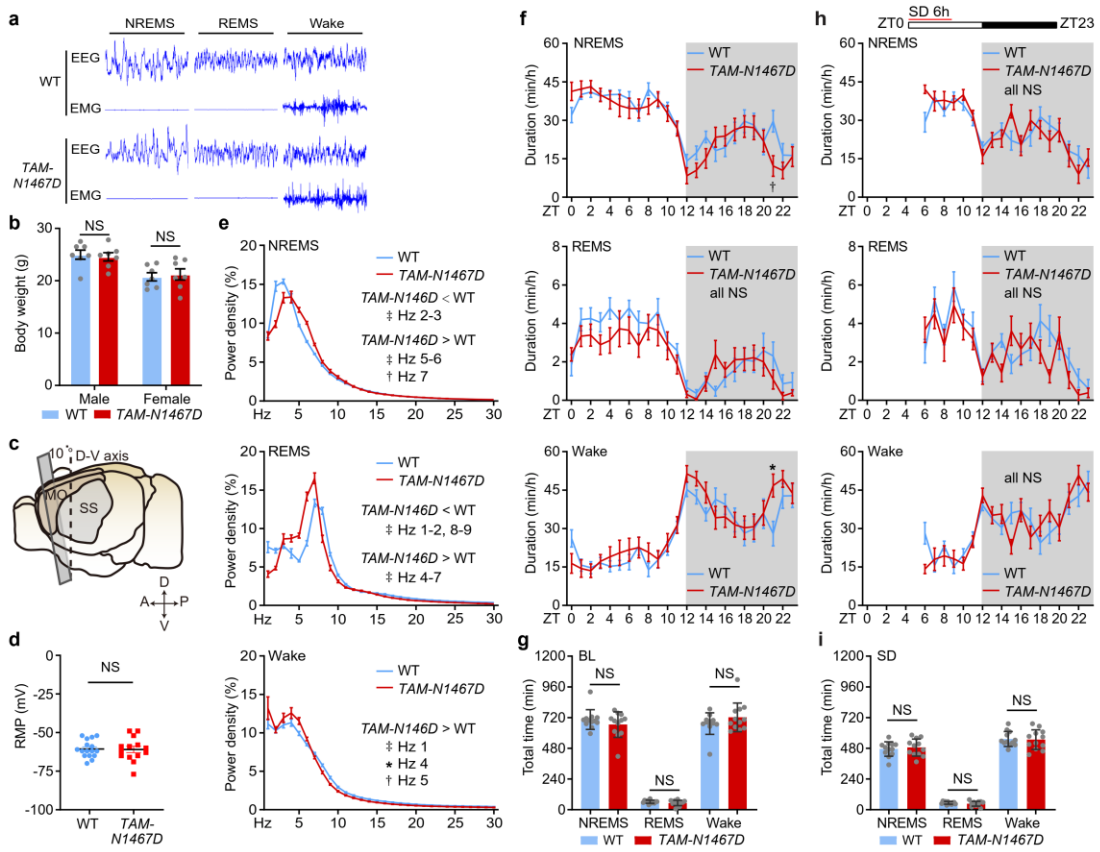

Extended Data Fig. 7 Sleep analysis of *TAM-N1467D* mice.

a-b. Representative 8-s EEG/EMG traces **(a)** and body weight comparison between WT and *TAM-N1467D* mice **(b,** n= 7 each).

c-d. Schematic of brain slice sampling (**c**, slicing plane tilted forward by 10°. MO, motor cortex. SS, somatosensory cortex), and resting membrane potential (RMP) of neurons from WT and *TAM-N1467D* mice (**d**, 14 vs. 16).

e-i. Sleep analysis of WT *vs.* *TAM-N1467D* (n=12 each) mice. Relative EEG power spectrum **(e)**, hourly **(f)** and total **(g)** duration of NREMS, REMS, and wakefulness; hourly **(h)** and total **(i)** duration of NREMS, REMS, and wakefulness after 6 h SD.

Data: mean ± s.e.m. (**e, f, h**); mean ± s.d. (**d, g, i**). Two-way ANOVA (Sidak's: **e, f, h**); Two-tailed *t*-test (**b, d, g, i**).

* $P < 0.05$; † $P < 0.01$; ‡ $P < 0.001$; NS, not significant, $P > 0.05$.

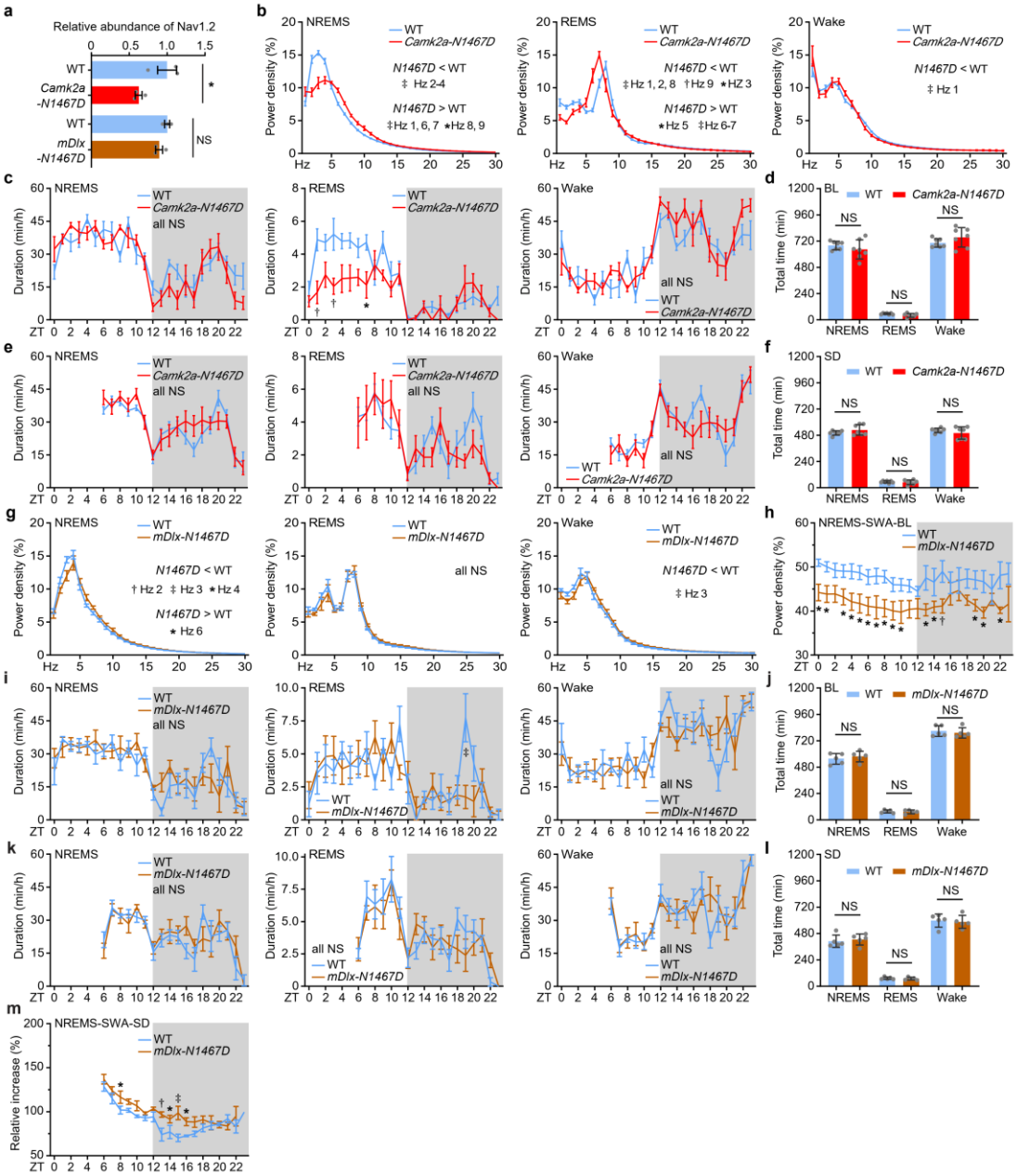

Extended Data Fig. 8 Sleep analysis of *Camk2a-N1467D* and *mDlx-N1467D* conditional mutant mice.

a. Brain Nav1.2 immunoblot quantification. WT *vs. Camk2a-N1467D*, *mDlx-N1467D* (n=3 each).

b-f. Sleep analysis of WT *vs. Camk2a-N1467D* (n=7 each) mice. Relative EEG power spectrum **(b)**, hourly **(c)** and total **(d)** duration of NREMS, REMS, and wakefulness; hourly **(e)** and total **(f)** duration of NREMS, REMS, and wakefulness after 6 h SD.

g-m. Sleep analysis of WT *vs. mDlx-N1467D* (n=5 each) mice. Relative EEG power spectrum **(g)**, baseline NREMS-SWA **(h)**, hourly **(i)** and total **(j)** duration of NREMS, REMS, and wakefulness; hourly **(k)** and total **(l)** duration of NREMS, REMS, and wakefulness, and rebound NREMS-SWA **(m)** after 6 h SD.

Data: mean ± s.e.m. **(b, c, e, g-i, k, m)**; mean ± s.d. (**d, f, j, l**). Two-way ANOVA (Sidak's: **b, c, e, g-i, k, m**); Two-tailed *t*-test (**d, f, j, l**).

* $P < 0.05$; † $P < 0.01$; ‡ $P < 0.001$; NS, not significant, $P > 0.05$.

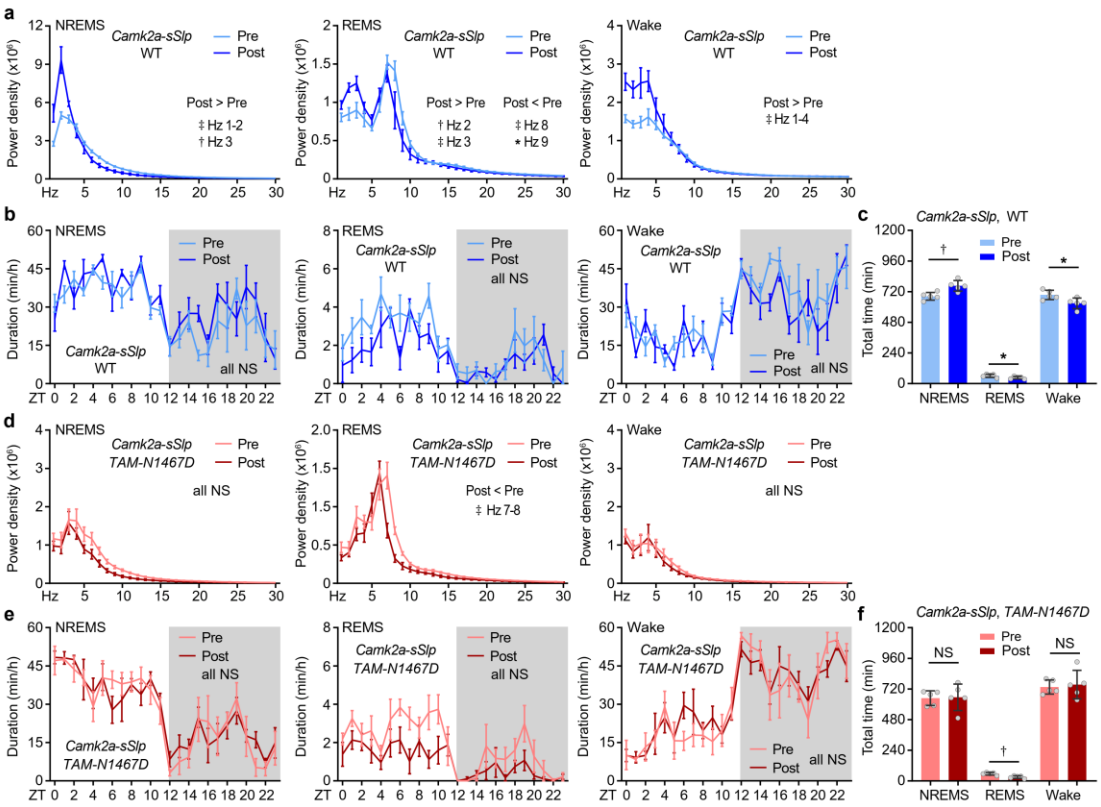

Extended Data Fig. 9 Sleep analysis of WT and *TAM-N1467D* mice expressing truncated SIK3 protein.

a-c. Sleep analysis of WT mice expressing sSLP (n=5). Relative EEG power spectrum **(a)**, hourly **(b)** and total **(c)** duration of NREMS, REMS, and wakefulness.

d-f. Sleep analysis of TAM-N1467D mice expressing sSLP (n=5). Relative EEG power spectrum **(d)**, hourly **(e)** and total **(f)** duration of NREMS, REMS, and wakefulness.

Data: mean ± s.e.m. (**a, b, d, e**); mean ± s.d. (**c, f**). Two-way ANOVA (Sidak's: **a, b, d, e**); Two-tailed *t*-test (**c, f**).

* $P < 0.05$; † $P < 0.01$; ‡ $P < 0.001$; NS, not significant, $P > 0.05$.

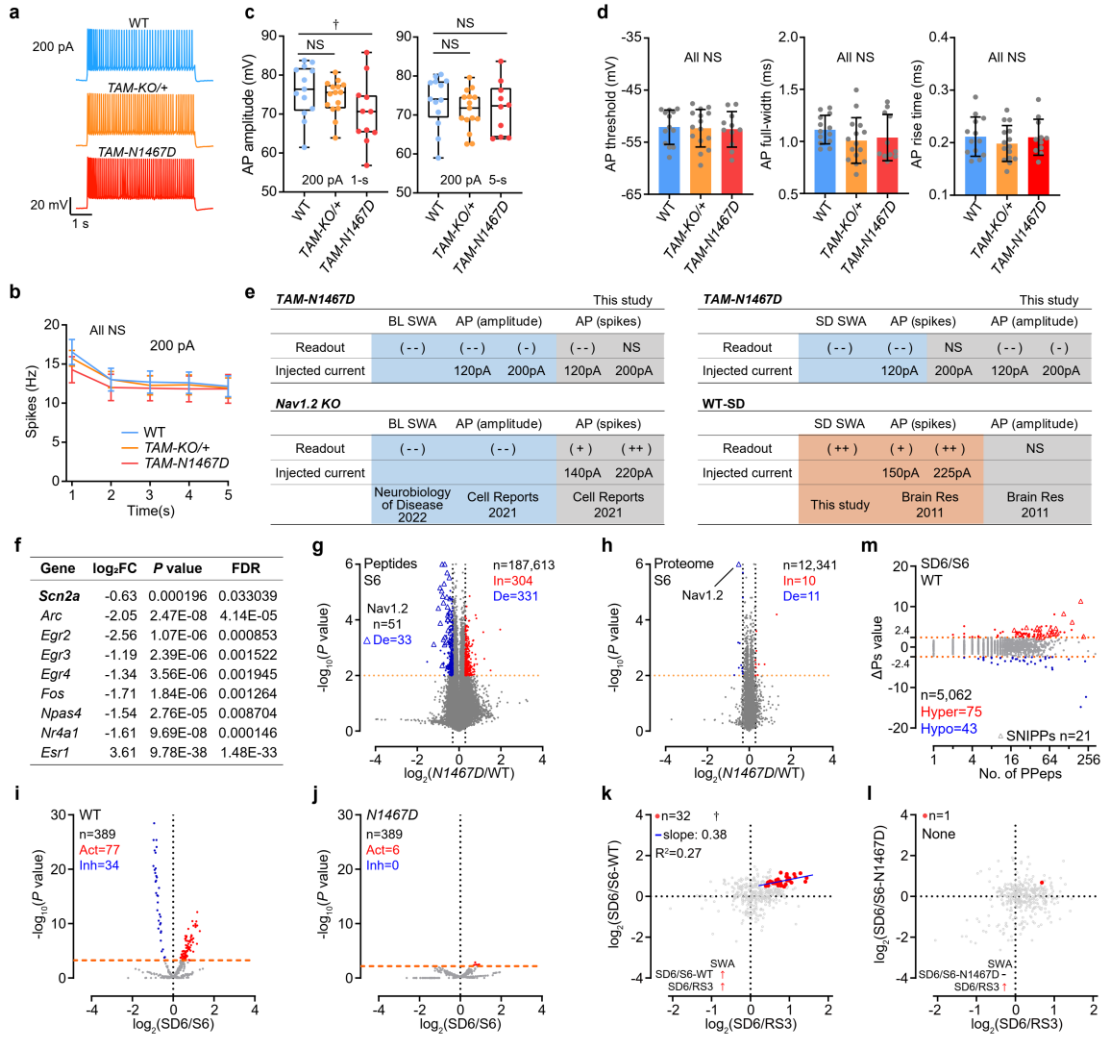

Extended Data Fig. 10 Electrophysiological and phosphoproteomic analysis of *TAM-N1467D* mice.

a-c. Evoked responses to a 5-s 200 pA depolarizing step **(a)**, spike counts per second **(b)**, AP amplitude quantified during the 1-s and 5-s epochs at 200 pA **(c)**. WT (n = 13), *TAM-KO/+*(n = 15), *TAM-N1467D* (n = 11)

d. AP threshold (left), AP full-width at half-maximum (middle), and rise time at rheobase current (right). WT (n = 13), *TAM-KO/+*(n = 15), *TAM-N1467D* (n = 11).

e. Cross-reference comparing neuronal excitability and NREMS-SWA changes.

f-h. Representative RNA expression changes **(f)**, peptides **(g)** and proteins **(h)** volcano plots for N1467D/WT (S6) comparison.

i-m. Kinase motif enrichment **(i, j)**, and correlation analysis of significantly altered kinases. SD6/RS3 *vs.* SD6/S6-WT **(k)**, SD6/S6-N1467D **(l)**, and global ΔPs analysis of SD6/S6-WT **(m)**.

Act, activated. Inh, inhibited.

Data: mean ± s.e.m. (**b**); mean ± s.d. (**d, g**). Two-way ANOVA (Fisher's LSD: **b**); Ordinary

one-way ANOVA (Fisher's LSD: **c, d**).

* $P < 0.05$; NS, not significant, $P > 0.05$.

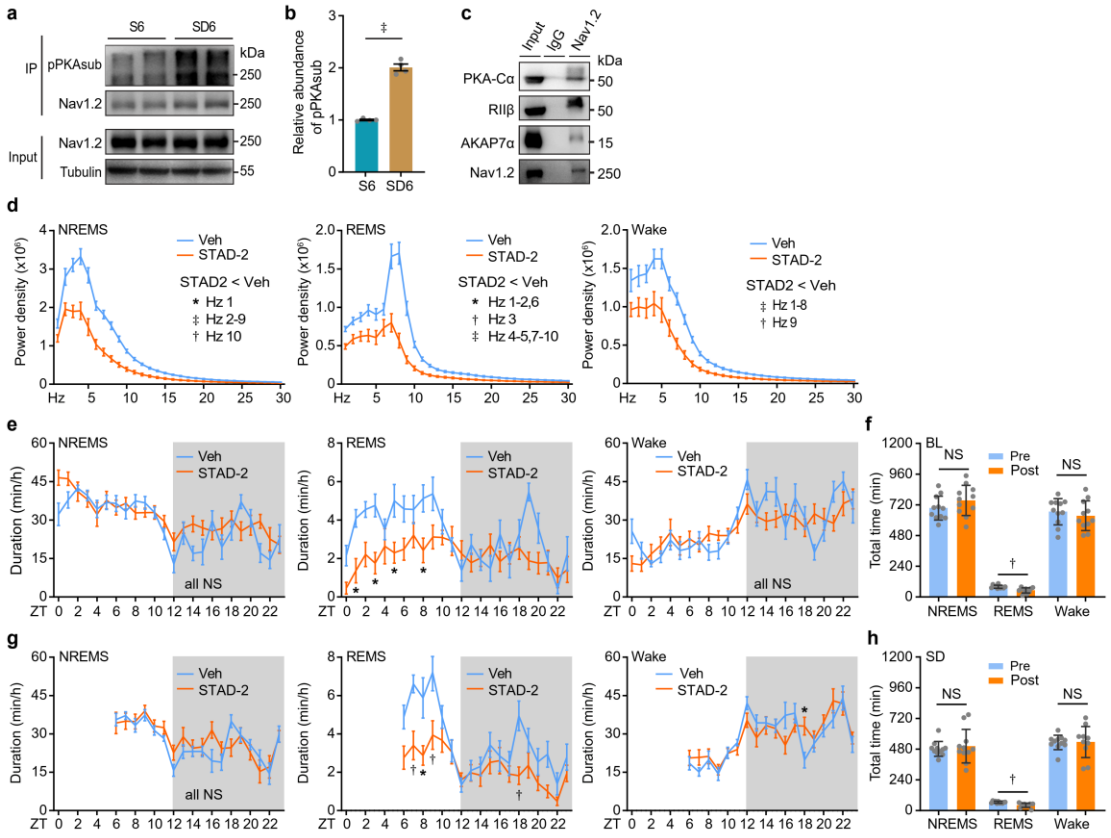

Extended Data Fig. 11 Sleep analysis of WT mice injected with STAD-2.

a-c. Representative immunoblots **(a)** and quantitative analysis **(b)** of PKA substrate motif (pPKAsub) in Nav1.2 immunoprecipitates (S6 vs. SD6, n=4 each), and Co-IP analysis of Nav1.2-associated proteins **(c)**.

d-h. Sleep analysis of WT mice (Veh *vs.* STAD-2, n=11). EEG power spectrum **(d)**, hourly **(e)** and total **(f)** duration of NREMS, REMS, and wakefulness; hourly **(g)** and total **(h)** duration of NREMS, REMS, and wakefulness after 6 h SD.

Data: mean ± s.e.m (**d-e, g**); mean ± s.d. (**f, h**). Two-way ANOVA (Sidak's: **d-e, g**); Two-tailed *t*-test (**f, h**).

* $P < 0.05$; † $P < 0.01$; ‡ $P < 0.001$; NS, not significant, $P > 0.05$.

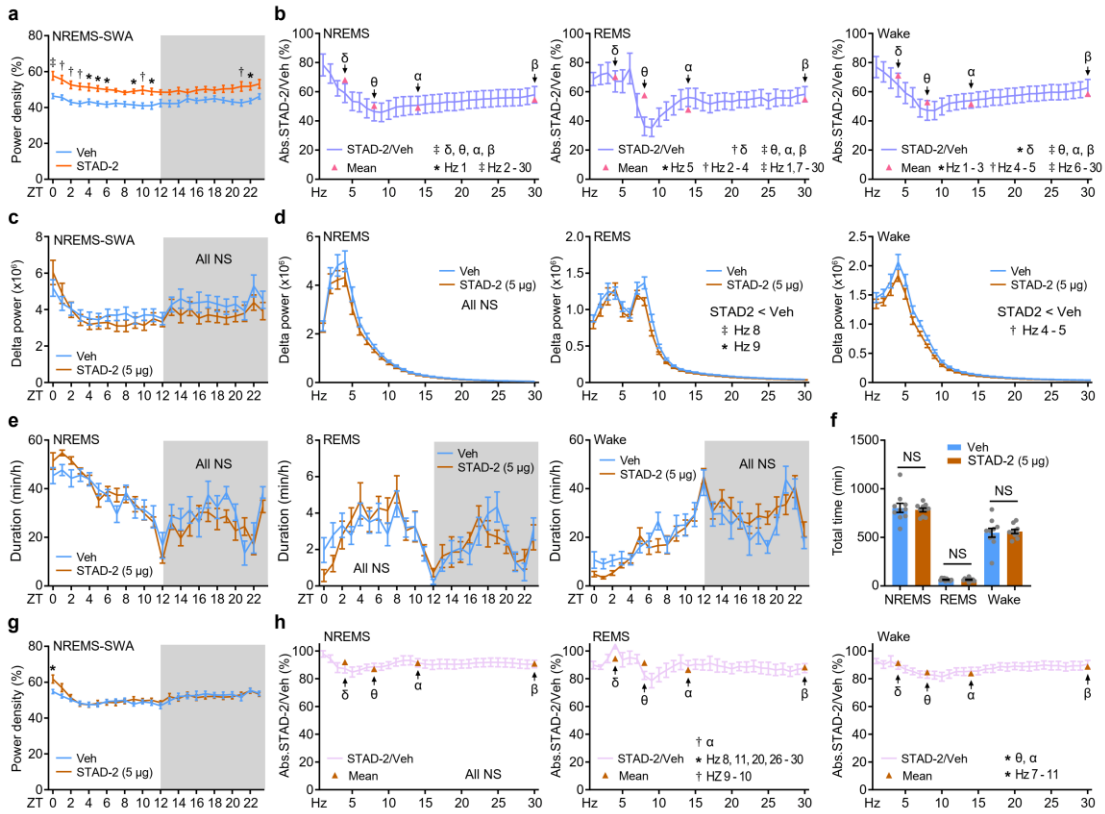

Extended Data Fig. 12 Effects of STAD-2 dose on sleep EEG power in mice

a-b. Sleep analysis of WT mice treated with vehicle (Veh) or STAD-2 (10 μg, n=11). **(a)** Baseline NREMS-SWA analysis using relative EEG power density; **(b)** absolute EEG power changes (STAD-2/Veh ratio) for 1-30 Hz and specific frequency bands.

c-g. Sleep analysis of WT mice treated with 5 μg STAD-2 (n=10). **(c)** Baseline NREMS-SWA analysis using absolute EEG power density; **(d)** absolute EEG power spectrum, **(e)** hourly and **(f)** total duration of NREMS, REMS, and wakefulness; **(g)** Baseline NREMS-SWA analysis using relative EEG power density; **(h)** absolute EEG power changes (STAD-2/Veh ratio) for 1-30 Hz and specific frequency bands.

Data: mean ± s.e.m. (**a-h**). Two-way ANOVA (Sidak's test: **a, c-e, g**); Two-tailed *t*-test **(b, f, h)**.

* $P < 0.05$; † $P < 0.01$; ‡ $P < 0.001$; NS, not significant, $P > 0.05$.

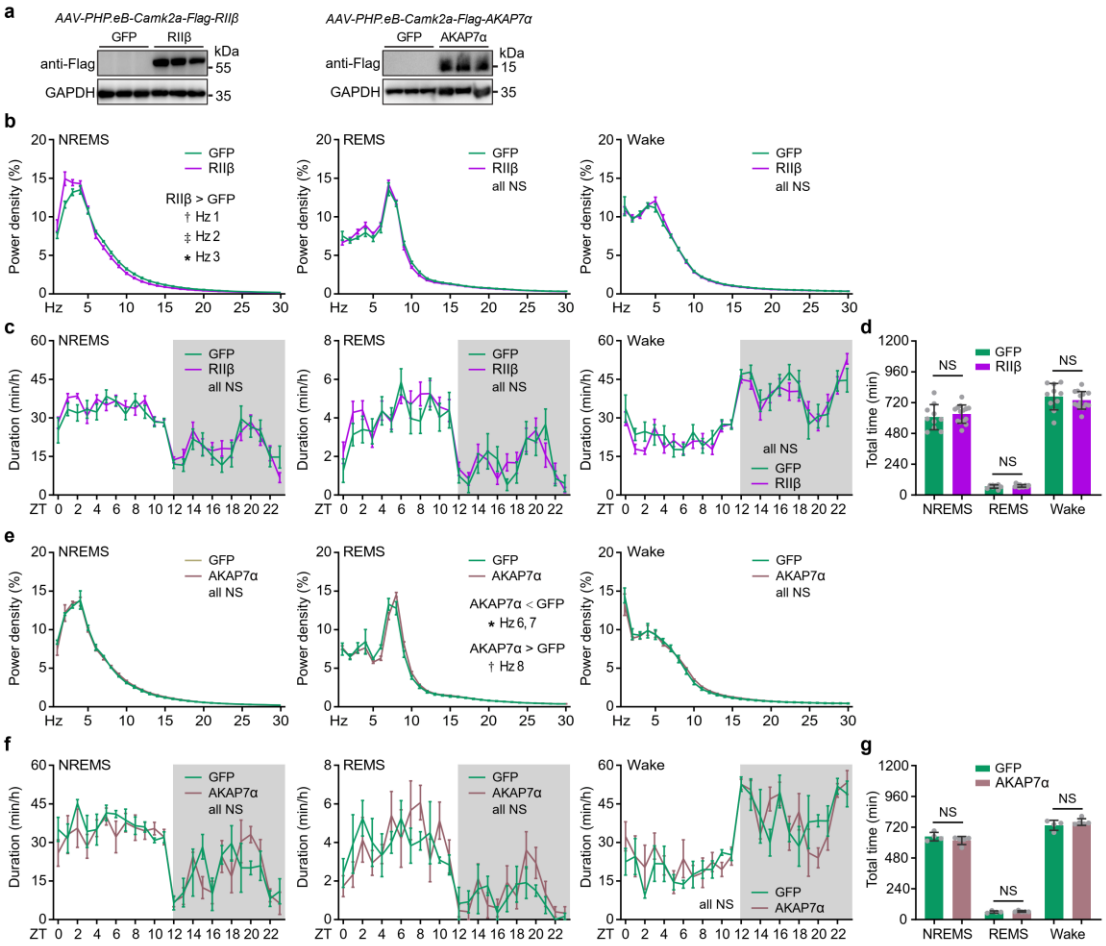

Extended Data Fig. 13 Sleep analysis of WT mice expressing RIIβ or AKAP7α.

a-g. Representative immunoblots **(a)**; sleep analysis of WT mice expressing RIIβ or AKAP7α, relative EEG power spectrum **(b, e)**, hourly **(c, f)** and total **(d, g)** duration of NREMS, REMS, and wakefulness. GFP *vs.* RIIβ (10 vs. 14); GFP *vs.* AKAP7α (4 vs. 5).

Data: mean ± s.e.m. (**b, c, e, f**); mean ± s.d. (**d, g**). Two-way ANOVA (Sidak's: **b, c, e, f**); Two-tailed *t*-test (**d, g**).

* $P < 0.05$; † $P < 0.01$; ‡ $P < 0.001$; NS, not significant, $P > 0.05$.

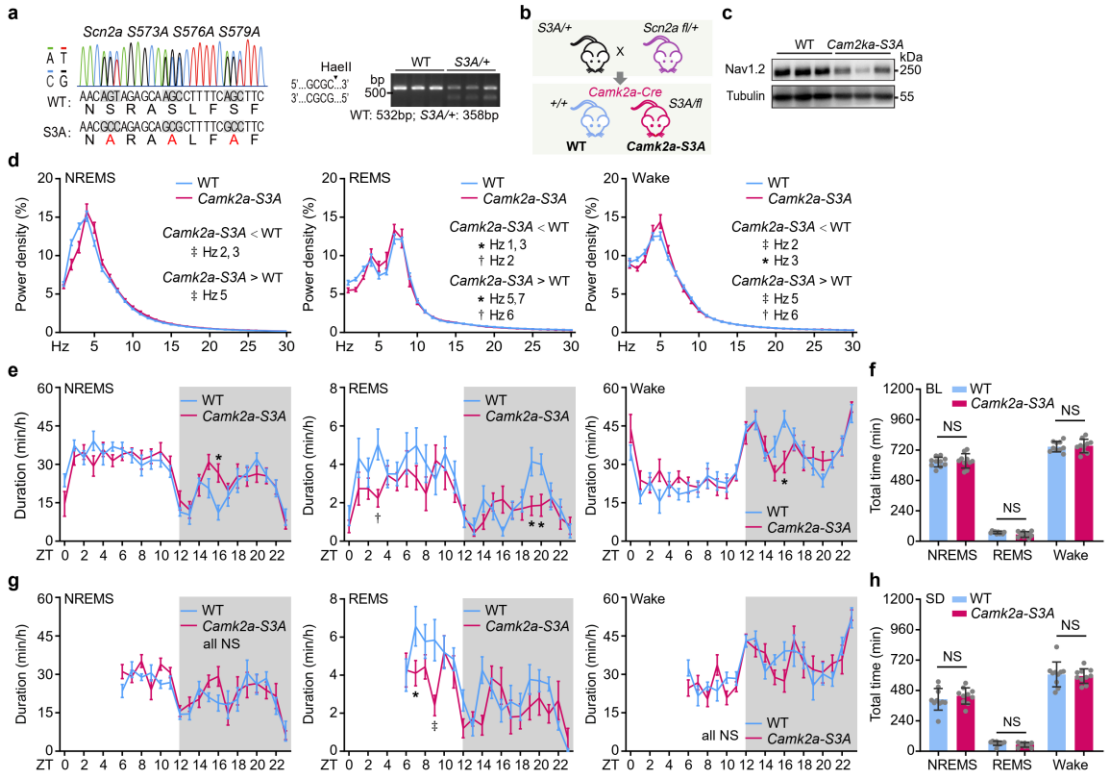

Extended Data Fig. 14 Sleep analysis of *Camk2a-S3A* mice.

a. Direct sequencing, genotyping designs, and RT-PCR analysis of the *S3A/+* mutant mouse. **b-c.** Schematic of the breeding strategy **(b)**, and immunoblot of brain Nav1.2 abundance of *Camk2a-S3A* mice **(c)**.

d-h. Sleep analysis of WT *vs. Camk2a-S3A* (n=10 each) mice. Relative EEG power spectrum **(d)**, hourly **(e)** and total **(f)** duration of NREMS, REMS, and wakefulness; hourly **(g)** and total **(h)** duration of NREMS, REMS, and wakefulness after 6 h SD.

Data: mean ± s.e.m. (**d, e, g**); mean ± s.d. (**f, h**). Two-way ANOVA (Sidak's: **d, e, g**); Two-tailed *t*-test (**f, h**).

* $P < 0.05$; † $P < 0.01$; ‡ $P < 0.001$; NS, not significant, $P > 0.05$.

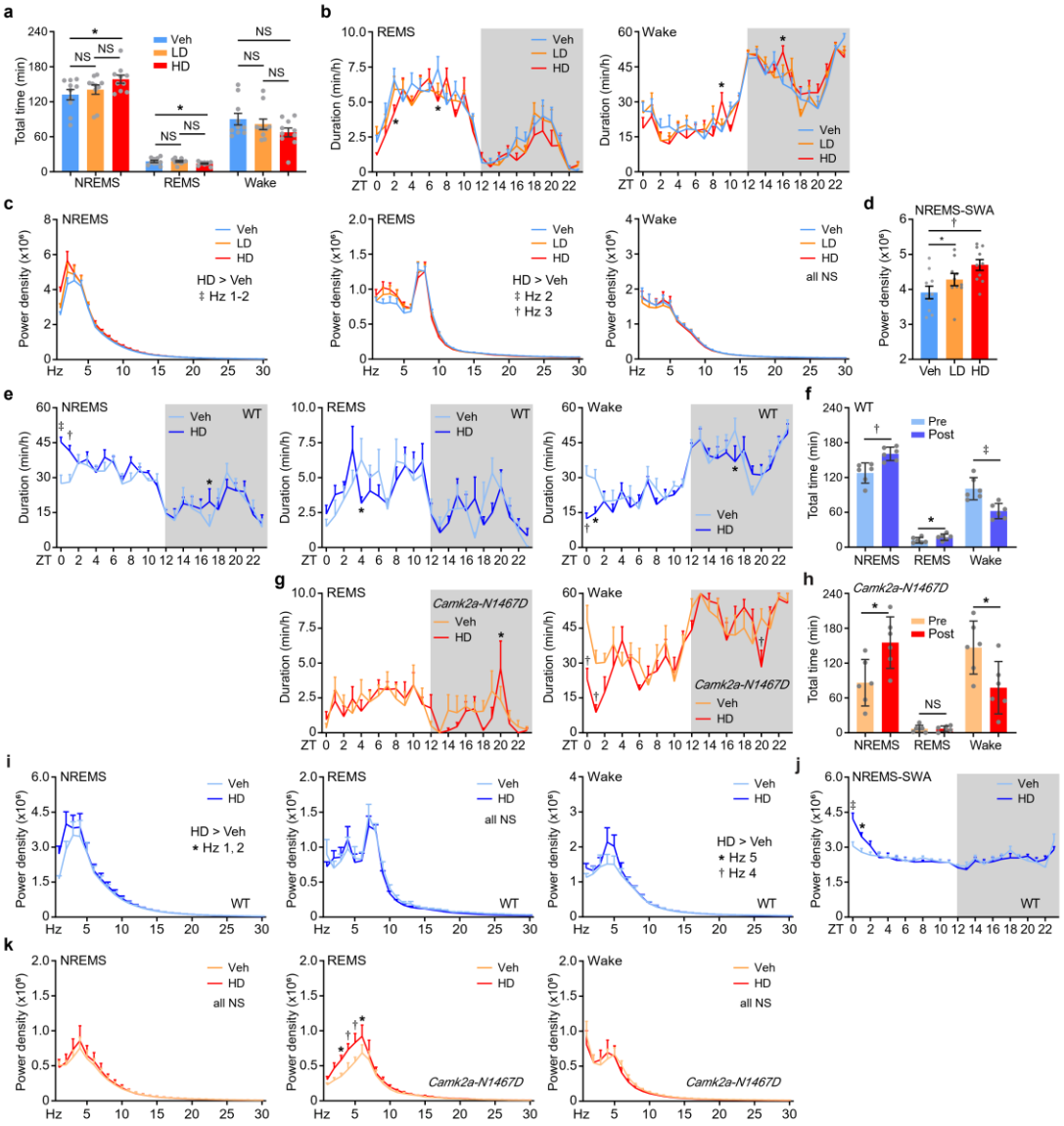

Extended Data Fig. 15 Sleep analysis of WT and *Camk2a-N1467D* mice injected with gabapentin.

a-d. Sleep analysis of WT mice (Veh *vs.* LD, HD gabapentin, n=10): total **(a)** and hourly **(b)** duration of NREMS, REMS, and wakefulness, relative EEG power spectrum **(c)**, and quantitative analysis of baseline NREMS-SWA **(d)**.

e-h. Circadian **(e, g)** and quantitative **(f, h)** analyses of baseline NREMS in WT and *Camk2a-N1467D* mice injected with Veh and HD-GBP (n=6 each).

i-k. Relative EEG power spectrum **(i, k)** and baseline NREMS-SWA **(j)** in WT and *Camk2a-N1467D* mice injected with Veh and HD-GBP.

Data: mean ± s.e.m. (**b**, **c**, **e**, **g**, **i-k**); mean ± s.d. (**a**, **d**, **f**, **h**). Repeated measures (RM) one-way ANOVA (Fisher's LSD: **a, d**); Two-way ANOVA (Dunnett's: **b-c**; Fisher's LSD: **e, g**; Sidak's: **i-k**); Two-tailed *t*-test (**f, h**).

* $P < 0.05$; † $P < 0.01$; ‡ $P < 0.001$; NS, not significant, $P > 0.05$.